The Astrophysical Journal, 998:117 (29pp), 2026 February 10 https://doi.org/10.3847/1538-4357/ae27c5

The Apache Point Observatory Extra-galactic Evolution Experiment (APOeGEE): Chemical Abundance Trends for Seven Dwarf Spheroidal Galaxies in the APOGEE Survey

Matthew Shetrone[1], Rachael L. Beaton[2], Christian R. Hayes[2], Sten Hasselquist[2], Joshua D. Simon[3], Jon A. Holtzman[4], Katia Cunha[5,6], Steven R. Majewski[7], Jennifer Sobeck[8], Ricardo Schiavon[9], Thomas Masseron[10,11], Verne V. Smith[12,13], and David L. Nidever[14]
[1] University of California Observatories, University of California Santa Cruz, Santa Cruz, CA 95064, USA
[2] Space Telescope Science Institute, 3700 San Martin Drive, Baltimore, MD 21218, USA
[3] Observatories of the Carnegie Institution for Science, 813 Santa Barbara Street, Pasadena, CA 91101, USA
[4] Department of Astronomy, New Mexico State University, P.O.Box 30001, MSC 4500, Las Cruces, NM 88003, USA
[5] Observatório Nacional/MCTI, R. Gen. José Cristino, 77, 20921-400, Rio de Janeiro, Brazil
[6] Steward Observatory, University of Arizona Tucson, AZ 85719, USA
[7] Department of Astronomy, University of Virginia, Charlottesville, VA 22904, USA
[8] Department of Astronomy, University of Washington, Box 351580, Seattle, WA 98195, USA
[9] Liverpool John Moores University: Liverpool, Merseyside, GB, UK
[10] Instituto de Astrofísica de Canarias (IAC), E-38205 La Laguna, Tenerife, Spain
[11] Universidad de La Laguna (ULL), Departamento de Astrofísica, 38206, La Laguna, Tenerife, Spain
[12] NOIRLab, Tucson, AZ 85719, USA
[13] Institut d'Astrophysique de Paris, UMR 7095 CNRS & Sorbonne Université, 98 bis Boulevard Arago, Paris 75014, France
[14] Department of Physics, Montana State University, P.O. Box 173840, Bozeman, MT 59717-3840, USA
Received 2025 September 19; revised 2025 November 5; accepted 2025 November 5; published 2026 February 5

Abstract

In addition to comprehensive surveys of the Milky Way (MW) bulge, disk, and halo, the Apache Point Galactic Evolution Experiment (APOGEE) project observed seven dwarf spheroidal satellites (dSphs) of the MW: Carina, Sextans, Sculptor, Draco, Ursa Minor, Bootes 1, and Fornax. APOGEE radial velocities, stellar parameters, and Gaia EDR3 proper motions are used to identify member stars from the targets in the vicinity of each dwarf; for seven dwarfs, new member stars are identified. To properly analyze the abundance patterns of these galaxies, a novel procedure was developed to determine the measurable upper limits of the APOGEE chemical abundances as a function of the effective temperature and the spectral signal-to-noise ratio. In general, the APOGEE abundance patterns of these galaxies (limited to $[Fe/H] > -2.5$) agree with those found in high-resolution optical studies in the literature after abundance offsets are applied. Most of the galaxies studied here have abundance patterns that are distinctly different from the majority of stars found in the MW halo, suggesting that these galaxies contributed little to the MW halo above $[Fe/H] > -2.0$. From these abundance patterns, we also find that these dSphs tend to follow two types of chemical evolution paths: episodic and continuous star formation, a result that is broadly consistent with previous photometric studies of the star formation histories (SFHs) of these galaxies. We explore whether mass and/or environment have an impact on whether a galaxy has an episodic or continuous SFH, finding tentative evidence that, in addition to the galaxy's mass, proximity to a larger galaxy and the cessation of star formation may drive the overall shape of the chemical evolution.

Unified Astronomy Thesaurus concepts: Galaxy abundances (574); Galaxy chemical evolution (580); Dwarf galaxies (416)

Materials only available in the online version of record: figure set, machine-readable table

1. Introduction

Detailed chemical abundances determined from high-resolution spectroscopy of even small numbers of stars in dwarf Spheroidal (dSph) galaxies (e.g., M. D. Shetrone et al. 2001; M. Shetrone et al. 2003) have long demonstrated that these objects are predominantly metal-poor ($[Fe/H] < -0.5$ for most dSphs) and often have significant enhancements in their α-elements ($[\alpha/Fe] > +0.4$) at $[Fe/H] < -2.0$. Decades later, the number of stars in individual dwarf galaxies with measured chemical patterns remains small (notable exceptions being B. Letarte et al. 2010; B. Lemasle et al. 2014; V. Hill et al. 2019; R. Theler et al. 2020; S. Vitali et al 2025, with as many as ~100 stars) with the largest literature compilations consisting of 1058 unique stars across 25 galaxies (T. Suda et al. 2008, 2011; S. Yamada et al. 2013; T. Suda et al. 2017). In addition, many of the objects were targeted for having extraordinary properties, such as being extremely metal-poor (e.g., J. G. Cohen & W. Huang 2010; J. E. Norris et al. 2010a, 2010b; M. Tafelmeyer et al. 2010; P. Jablonka et al. 2015; J. D. Simon et al. 2015; Á. Skúladóttir et al. 2021) or exhibiting peculiar element enhancements (e.g., A. P. Ji et al. 2023). Even when ensembles of stars in the literature can be compiled, these compilations consist of observations using different instrumental setups and often contain a wide range of different abundance analysis procedures, all of which can lead to significant systematic uncertainties in a compiled chemical dataset. Lastly, relatively few studies of dwarf spheroidal

satellites (dSphs) also study significant samples of Milky Way (MW) stars, making it difficult to compare and contrast the abundance-inferred star formation histories (SFHs) of the dSphs to each other and to the MW, particularly to the halo of the MW. Therefore, open questions remain about how these galaxies may have formed stars differently, both early on in their formation and at more recent times, when their interactions with the MW (and in some cases each other) either stalled or restarted star formation.

An ideal chemical abundance study of these dSph galaxies would then consist of observations from a single instrument with stellar parameters and abundances derived in a homogeneous way. Such a survey at high resolution is nearly time-prohibitive without dedicated multiyear surveys, but such a dataset was obtained by E. N. Kirby et al. (2010) using low-resolution spectroscopy ($R \simeq 6000$) of several hundred stars across (Sculptor, Fornax, Leo I, Sextans, Leo II, Canes Venatici I, Ursa Minor, and Draco). From the metallicity distribution functions of these galaxies, E. N. Kirby et al. (2011b) concluded that the more luminous dwarf galaxies tended to enrich to higher metallicity, suggesting that more-massive galaxies better retain gas that can then be used to continue star formation. From the [α/Fe]–[Fe/H] abundance patterns of these dSphs, they found that all galaxies had Type Ia supernovae (SNe) contributing to the chemical abundances of most stars at [Fe/H] > -2.5 (E. N. Kirby et al. 2011a), in stark contrast to the MW. They also used chemical evolution models to investigate whether some of the dSph galaxies showed chemical signatures of starbursts. Although the Kirby et al. studies have been monumental in providing a more universal picture of how these dwarf galaxies form and evolve over time, additional details can be inferred from the measurements of individual chemical abundances, which are typically accessible to higher precision at higher spectral resolution (although they were able to measure some individual elements; e.g., E. N. Kirby et al. 2009, 2011b).

In this work, we extend the work on Local Group dwarf galaxies of S. Hasselquist et al. (2017), D. L. Nidever et al. (2020), and S. Hasselquist et al. (2021) by presenting detailed chemical abundances of up to 12 elements for 537 stars across seven dSphs: Carina, Sextans, Sculptor, Draco, Ursa Minor, Bootes 1, and Fornax. These abundances were measured from spectra obtained by the Apache Point Galactic Evolution Experiment (APOGEE), which was a high-resolution ($R \simeq$ 20,000) near-infrared (NIR) spectroscopic (S. R. Majewski et al. 2017) survey of stars across the MW and its satellite galaxies. Although fainter than the typical APOGEE target, deep observations were able to target the upper red giant branch of these systems. However, the varying signal-to-noise ratio (S/N) and metal-poor nature of these observations require careful analysis and discriminating between true measurements and upper limits. In this study, we derive a prescription for determining upper limits on abundances based on the S/N of the observation and stellar parameters of the star. We used these abundance upper limits to better analyze the chemical abundance patterns of the dSph galaxies at [Fe/H] > -2.5, but these upper limits could, in principle, be applied to all APOGEE results. The data used and the target selection are described in Section 2. Stellar parameters and abundance determination, along with the prescription for upper limits, are discussed in Section 3. The chemical abundance patterns for the 7 dSphs are presented in Section 4, and comparisons with optical literature samples are shown in Section 5. We discuss what these chemical abundance patterns of the dSphs mean for their detailed SFHs in Section 6, dividing the dSphs into two groups based on whether they have had continuous or episodic SFHs, as indicated by their chemical abundance patterns.

2. Data Source and Target Selection

For our dSph sample, we start with data from the 17th Data Release (DR17; Abdurro'uf et al. 2021) of the fourth iteration of the Sloan Digital Sky survey (SDSS-IV; M. R. Blanton et al. 2017), making use of the spectroscopic observations from the twin APOGEE spectrographs (J. C. Wilson et al. 2019) on board the Apache Point Observatory SDSS 2.5 m (J. E. Gunn et al. 2006) and Las Campanas Observatory 2.5 m (I. S. Bowen & A. H. Vaughan 1973) telescopes, referred to as APOGEE-N and APOGEE-S, respectively. These spectrographs obtained *H*-band spectra of ~750,000 stars across the MW and its nearby satellite galaxies. We first describe how the dSphs were initially targeted in Section 2.1, and describe how we selected the most likely members of the dSphs from these observations in Section 2.2.

2.1. Target Selection for APOGEE Survey

Targeting dSph stars in any project is complex because of their low stellar density, subjecting them to MW foreground contamination, and given their large distances, their stars are quite faint. Both concerns are relevant for APOGEE. With only a 2.5 m aperture, even stars at the tip of the red giant branch (TRGB) require more than 20 hr of integration to reach a sufficient S/N for spectral synthesis analysis (typically around an S/N of 70; e.g., H. Jönsson et al. 2020). The long integration time required means that only a single dedicated field would be designed for each dSph, Moreover, the fiber-collision limits for APOGEE are larger than other dSph spectroscopic surveys; two fibers in APOGEE can only be placed as close as 71.″5 for the APOGEE-N instrument and 56″ on the APOGEE-S instrument. The field of view for APOGEE is sufficiently large to span nearly the full sizes of many dSphs with a 1.°5 radius for APOGEE-N and 0.°95 radius for APOGEE-S.[15] These targeting constraints mean that there were fibers that could not be assigned to dSph targets, and some bright dSph stars could not be observed. All of these factors meant that target selection for these fields differed substantially from typical APOGEE survey target selection described in G. Zasowski et al. (2013) and G. Zasowski et al. (2017).

With all of these constraints, only seven of the many Milky Way dSphs could be readily targeted by APOGEE-2: Draco, Ursa Minor, and Bootes I with APOGEE-N and Fornax, Sculptor, Carina, and Sextans with APOGEE-S. We note that, as described in F. A. Santana et al. (2021), Fornax was added to the dSph program later in the design of the survey and could therefore make use of Gaia proper-motion measurements; the other dSph target selection was completed before Gaia DR2. All plates were originally scheduled for 24 visits, roughly 24 hr, of on-sky time with an additional 12 hr granted as part of the Bright Time Extension for dSphs observed at APO (R. L. Beaton et al. 2021). We note that some targets in Ursa

[15] We note that APOGEE-S also has two large obscured regions for the positioning and guiding optics that block parts of the field of view. See F. A. Santana et al. (2021) for a detailed description.

Table 1
Membership Criteria

DR17 MEMBER dSph Membership Criteria

dSph	Central Coord.		Tele.	Radius	v_{sys}	Δ_{RV}	Proper Motion[b]	
	(deg)	(deg)		(arcmin)	(km s^{-1})	(km s^{-1})	(mas yr^{-1})	(mas yr^{-1})
Bootes I	210.024994	14.500000	N	90.	99.0	50.	−0.46 ± 0.16	−1.06 ± 0.16
Carina	100.835228	−51.099789	S	90.	229.0	50.	0.50 ± 0.10	−0.14 ± 0.10
Draco	260.049988	57.915001	N	90.	−291.0	50.	−0.02 ± 0.14	−0.14 ± 0.14
Fornax	39.995800	−34.449001	S	90.	55.3	50.	0.38 ± 0.07	−0.41 ± 0.07
Sculptor	15.220700	−33.688961	S	90.	111.4	50.	0.08 ± 0.12	−0.13 ± 0.12
Sextans	153.262497	−1.614700	S	90.	224.0	50.	−0.50 ± 0.12	0.08 ± 0.12
Ursa Minor	227.283325	67.222504	N	90.	−247.0	50.	−0.18 ± 0.14	0.07 ± 0.14

Final Criteria Adopted in This Work

dSph	Median Coord.		Tele.	Radius[a]	RV_{Median}	RV_{SMAD}	Proper Motion[b]	
	(deg)	(deg)		(arcmin)	(km s^{-1})	(km s^{-1})	(mas yr^{-1})	(mas yr^{-1})
Bootes I	210.131	14.598	N	⋯	101.11	4.57	−0.37 ± 0.047	−1.05 ± 0.054
Carina	100.359	−50.9635	S	⋯	224.5	5.53	0.558 ± 0.062	0.128 ± 0.079
Draco	259.978	57.9379	N	⋯	−293.07	10.47	0.032 ± 0.073	−0.181 ± 0.089
Fornax	39.9322	−34.5463	S	⋯	54.07	10.05	0.384 ± 0.066	−0.381 ± 0.104
Sculptor	15.0002	−33.7103	S	⋯	110.53	9.43	0.098 ± 0.072	−0.167 ± 0.056
Sextans	153.294	−1.5986	S	⋯	225.43	8.56	−0.405 ± 0.125	0.013 ± 0.135
Ursa Minor	227.415	67.2545	N	⋯	−246.85	7.43	−0.105 ± 0.096	0.08 ± 0.075

Notes.
[a] No spatial restrictions were used, but the plate radius formally limits this value.
[b] Proper motion of our sample, there are significantly more accurate proper motions in the literature (e.g., A. B. Pace et al. 2022).

Minor and Draco received up to 48 visits over the course of the APOGEE survey.

The targeting occurred in three primary phases: (1) selection of previously confirmed radial velocity members, (2) selection of high-likelihood red giant members selected using the Washington+DDO51 pre-selection (S. R. Majewski et al. 2000a), (3) selection of other candidate members using other external data. The selection of members relied heavily on prior spectroscopic work, in particular the radial velocities, and these stars have target flags of APOGEE_DSPH_MEMBER.

The selection of candidates beyond those targets already identified in the literature relied most heavily on Washington photometry, some of which was acquired for APOGEE-2 (J. Munn, private communication; Bootes I, Sextans) and some of which was available in the existing literature (for Carina, Ursa Major, Draco, and Sculptor; S. R. Majewski et al. 2000b; C. Palma et al. 2003; R. R. Muñoz et al. 2005; K. B. Westfall et al. 2006). In lieu of Washington photometry, Gaia DR2 proper motions (Gaia Collaboration et al. 2018) were used to select Fornax candidates. The Washington photometry allows for the selection of giants from foreground dwarfs of the same spectral type using the *DDO*51 intermediate-band filter centered on the surface-gravity sensitive Mgb spectral feature (S. R. Majewski et al. 2000a). Targets selected as candidate members based on external data are flagged as APOGEE_DSPH_CANDIDATE. Note that the targeting strategy described above means that our sample presented in this work cannot contain any potential young (∼1 Gyr old) stars that have been found in some of these galaxies (e.g., Y. Yang et al. 2024).

2.2. Selecting dSph Members in APOGEE DR17

Although the targeting strategy described in the previous section results in a high targeting fraction of available dSph members (described in detail in Section 2.2.1), we make use of APOGEE radial velocities and Gaia proper motions to ensure that the initial APOGEE targets are indeed members of these dSphs. APOGEE radial velocities are obtained for each visit using the methods described in D. L. Nidever et al. (2015). Much of this process was revised for DR17, partly inspired by the challenge of the low per-visit S/N of the dSph stars. These revisions are discussed in detail in J. A. Holtzman et al. (2025, in preparation) and used the Doppler[16] code (D. Nidever 2021). This code determines RVs through convolution followed by a series of cross correlations to spectral grids of increasing complexity generated by the Cannon (A. R. Casey et al. 2016). These RVs are combined with Gaia EDR3 proper motions and sky positions to create a "6σ Membership Sample," described in Section 2.2.2. The completeness of this sample is discussed in Section 2.2.3.

2.2.1. DR17 Membership Classifications

Our starting point for identifying members in the dSphs is the MEMBER tag included in the DR17 summary files. This tag combined a number of membership criteria to identify a set of the most likely members: (i) targets within 90′ of the dSph center, (ii) comparing the APOGEE vhelio_avg to the known systemic velocity of the dSph within 6σ of the cluster median, and (iii) comparing the target Gaia EDR3 proper motions to the known systemic proper motions of the dSph within 6σ of the cluster median values. The data used for these classifications are given in the top portion of Table 1 and a given APOGEE target has to meet all of the stated criteria to be flagged as a member in the MEMBER tag.[17]

[16] https://github.com/dnidever/Doppler
[17] Diagnostic figures affiliated with the MEMBER tag from the DR17 release can be found here: https://data.sdss.org/sas/dr17/apogee/spectro/redux/dr17/stars/dsph/.

Table 2
APOGEE dSph Sample

dSph		Kinematics[a]			ASPCAP[b]				Measurements[c]
	$N_{\rm Targets}$	$N_{\rm PM}$	$N_{\rm RV}$	$N_{\rm PM+RV}$	$N_{\rm ASPCAP}$	$N_{\rm CoolGiant}$	$N_{\rm M/H}$	$N_{\rm GoodASPCAP}$	$N_{\rm Fe}$
Bootes I	161	17	15	12	10	10	7	6	5
Carina	215	64	64	62	56	51	52	52	50
Draco	155	70	68	63	51	47	44	41	42
Fornax	248	239	247	239	212	203	211	209	208
Sculptor	238	208	204	201	181	173	168	161	149
Sextans	131	92	83	72	68	56	45	40	36
Ursa Minor	167	84	83	82	70	68	55	54	47
Total	1315	774	764	731	648	608	582	563	537

Notes.
[a] Using a 6σ window around the final criteria given in Table 1.
[b] See discussion in Section 3.1.
[c] Stars with detectable measurements in [Fe/H] as described in Section 3.2.

2.2.2. The 6σ Membership Sample

We provide an update to the MEMBER flag included in DR17 by extending our membership criteria to 6σ based on the median kinematic properties determined from the members: sky position, $v_{\rm sys}$, and proper motion; the parameters are given in Table 1. In particular, all 6σ members have original targeting flags of either APOGEE_DSPH_MEMBER, meaning it was an RV member in prior work, or APOGEE_DSPH_CANDIDATE, meaning that it had photometry properties consistent with being a metal-poor giant at the distance of the dSph. The exception is Fornax, whose candidate selection also included proper motions (details on Fornax selection are given in F. A. Santana et al. 2021). Thus, the membership used in this work does not exactly match the DR17 MEMBER flag. More details of these differences can be found in Appendix A.

As summarized in Table 2, there were 1315 stars targeted in the dSph program; of these, 530 (40%) were targeted as members of a dSph based on the results of the literature (primarily RVs) and 785 (60%) were candidate members using photometry or, for Fornax, proper motions. Applying the 6σ criteria in Table 1, 774 (59%) pass the proper-motion criteria, and 764 (58%) pass the RV criteria; combining the two, we have 731 stars meeting the kinematic membership cut (56%). No members were serendipitously identified, e.g., through the criteria of the "Main Red Star Sample" for a 24-visit field (G. Zasowski et al. 2013, 2017; R. L. Beaton et al. 2021; F. A. Santana et al. 2021); this is approximately consistent with the magnitude limits and the TRGB for the dSphs. In detailed inspection of the stellar spectra, 181 members (24%) are excluded from detailed chemical analyzes due to the poor quality of the spectra (see Section 3.1). We do find that some of our dSphs members exhibit RV variability consistent with having a binary companion, but an analysis of binaries in these dSphs is beyond the scope of this work.

Figure 1 provides a visual assessment of the final membership samples for each of the seven dSphs. Figure 1 has four panels: (a) spatial location compared to the plate radius (red) and the structural parameters of the dSph, (b) proper motion from Gaia EDR3 (Table 1), (c) radial velocity relative to the systemic velocity and the velocity dispersion, here plotted against projected distance from the dSph center, and (d) the Kiel diagram from APOGEE calibrated stellar parameters. The velocity dispersion and structural parameters for each dwarf were obtained from the updated compilation of A. W. McConnachie (2012);[18] the values and original references are provided in Table 3. These values of A. W. McConnachie (2012) are used only for visualization purposes, and these values did not affect the selection of members as described in Sections 2.2.1 and 2.2.2. As such, we note that there are more recent values for structural parameters such as S. A. Jenkins et al. (2021) for Bootes I, A. B. Pace et al. (2020) for Ursa Minor, and R. R. Muñoz et al. (2018) for several dwarfs, among others. In each panel of Figure 1, the open symbols do not meet the 6σ membership criteria, whereas the filled symbols do; orange symbols are those stars targeted as known members, and the blue symbols were selected as candidates.

2.2.3. Completeness

To understand the extent to which we are sampling the red giant branches of these dSphs, we show in Figure 2 a Gaia dereddened-color to absolute-magnitudes ($M_G = m_G - \mu_{\rm gal} - A_G$) diagram in the Gaia photometric bands for EDR3 for each dSph. The distances and reddening $E(B-V)$ adopted for Figure 2 are given in Table 3; these come from the compilation of A. W. McConnachie (2012) where $E(B-V)$ is from D. J. Schlegel et al. (1998). To place $E(B-V)$ in the Gaia filter system, we assume $R_V = 3.1$ and then follow S. Wang & X. Chen (2019), more specifically, $A_G = 0.789A_V$ and $E(BP-RP) = A_V/2.394$. The A_G ranges from 0.04 (Bootes I) to 0.15 mag (Carina), and the $E(BP-RP)$ varies from 0.02 (Bootes I) to 0.08 mag (Carina).

From Figure 2, we find that most dSphs, with the exception of Bootes I and Fornax, have $\sim$1.5 mag of their upper giant branch sampled. Sculptor exhibits the most "traditional" CMD consistent with simple chemical evolution, with a smooth metallicity gradient across the giant branch. Carina, despite being more metal-rich than Ursa Minor, has an RGB that is bluer than that of Ursa Minor. This suggests either that the adopted distance for one of the galaxies is incorrect or that the Carina stars are significantly younger than Ursa Minor. Strong evidence that Carina's stars are young comes from photometric studies (e.g., D. R. Weisz et al. 2014b). Such apparent age differences are discussed further in Section 4 after considering the chemical abundance trends.

[18] The 2021 updated compilation is available: https://www.cadc-ccda.hia-iha.nrc-cnrc.gc.ca/en/community/nearby/.

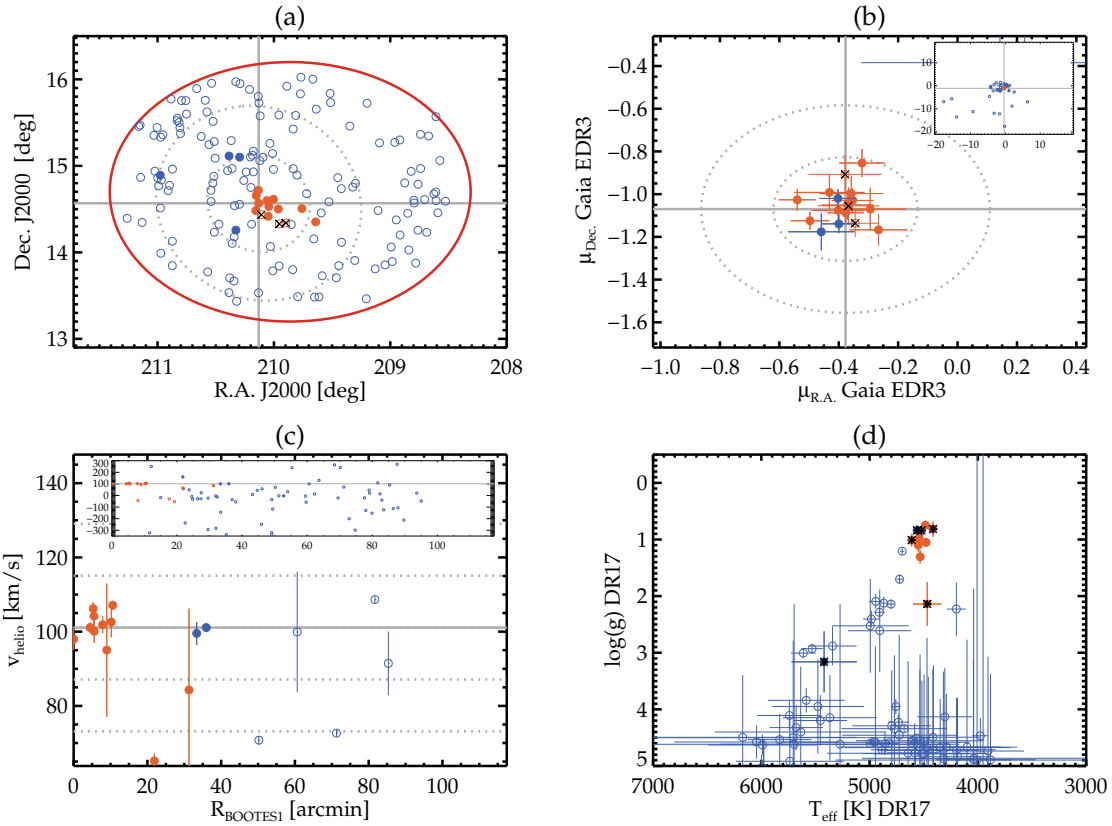

Figure 1. Four-panel targeting and membership demonstrations for all seven dSphs, in the following order: Bootes 1, Carina, Draco, Fornax, Sculptor, Sextans, and Ursa Minor. In all panels, dSph members are filled circles, and nonmembers are open circles. Stars targeted as literature members are in orange and candidates in blue, and targets with overall too low spectral quality to be evaluated confidently are indicated with a black "*x*." For each dSph, the panels are as follows: (a) Plate-centric sky distribution with the plate field of view in red, the central coordinates of the dSph are shown with the solid gray lines, and the 3 times and 6 times the half-light radius are indicated with dashed lines (structural parameters taken from the 2021 update to A. W. McConnachie 2012; see our Table 3). (b) Proper-motion distribution of targets; the central PM is given by the solid lines, and the circles represent 3σ and 6σ from the central value. The inset panel expands to a much larger PM range. (c) Radial velocity vs. the radial distance from the dwarf center with the central velocity from APOGEE DR17 RVs as solid lines and 3σ and 6σ given as dashed lines. The error bars plotted in this panel are VSCATTER that measures RV variability. The inset panel expands to a much larger RV range. (d) Kiel diagram for stars with calibrated ASPCAP results. Asterisks in this panel flag those stars with generally unreliable abundances.

(The complete figure set (7 images) is available in the online article.)

Table 3
dSph Properties

dSph	Distance[a]		$E(B-V)$[b]	PA[c]	ellip[c]	r_h[c]	σ[d]	M_*[e]	τ_{70}[e]
	(kpc)	(mag)	(mag)	(deg)		(arcmin)	(km s^{-1})	($10^6 M_\odot$)	$\log_{10}$ (yr)
Bootes I	66	$19.11^{0.08}_{0.08}$	0.017	7^{3}_{3}	$0.25^{0.02}_{0.02}$	$11.3^{0.27}_{0.27}$	$2.4^{0.9}_{0.5}$	0.029	10.12
Carina	105	$20.11^{0.13}_{0.13}$	0.061	60^{1}_{1}	$0.37^{0.01}_{0.01}$	$11.4^{0.12}_{0.12}$	$6.6^{1.2}_{1.2}$	0.38	9.56
Draco	76	$19.4^{0.17}_{0.17}$	0.027	97^{1}_{1}	$0.30^{0.01}_{0.01}$	$9.9^{0.09}_{0.09}$	$9.1^{1.2}_{1.2}$	0.29	10.03
Fornax	147	$20.84^{0.18}_{0.18}$	0.021	46^{1}_{1}	$0.28^{0.01}_{0.01}$	$18.4^{0.02}_{0.02}$	$11.7^{0.9}_{0.9}$	20.	9.67
Sculptor	86	$19.67^{0.14}_{0.14}$	0.018	94^{1}_{1}	$0.37^{0.01}_{0.01}$	$12.3^{0.05}_{0.05}$	$9.2^{1.4}_{1.4}$	2.3	10.06
Sextans	86	$19.67^{0.1}_{0.1}$	0.047	56^{5}_{5}	$0.35^{0.05}_{0.05}$	$27.8^{1.2}_{1.2}$	$7.9^{1.3}_{1.3}$	0.44	10.08
Ursa Minor	76	$19.4^{0.1}_{0.1}$	0.032	50^{1}_{1}	$0.55^{0.01}_{0.01}$	$17.3^{0.11}_{0.11}$	$9.5^{1.2}_{1.2}$	0.29	9.98

Notes.
[a] Distance Ref.—Boo: M. Dall'Ora et al. (2006); Car: G. Pietrzyński et al. (2009); Dra: A. Z. Bonanos et al. (2004); For: G. Pietrzyński et al. (2009); Scl: G. Pietrzyński et al. (2008); Sex: M. G. Lee et al. (2009); UMi: R. Carrera et al. (2002).
[b] Reddening Ref.—Taken from the position of the dSph in D. J. Schlegel et al. (1998) maps by A. W. McConnachie (2012).
[c] Struct. Param. Ref.—Boo: N. F. Martin et al. (2008); Car, For, Scl, Sex, UMi: M. Irwin & D. Hatzidimitriou (1995); Dra: N. F. Martin et al. (2008).
[d] σ Ref.—Boo: S. E. Koposov et al. (2011); Dra, UMi: M. I. Wilkinson et al. (2004); Car, For, Scl, Sex: M. G. Walker et al. (2008).
[e] Mass & τ_{70} Ref.—Car, Dra, For, Scl, UMi: D. R. Weisz et al. (2014a); Sex: M. Bettinelli et al. (2018).

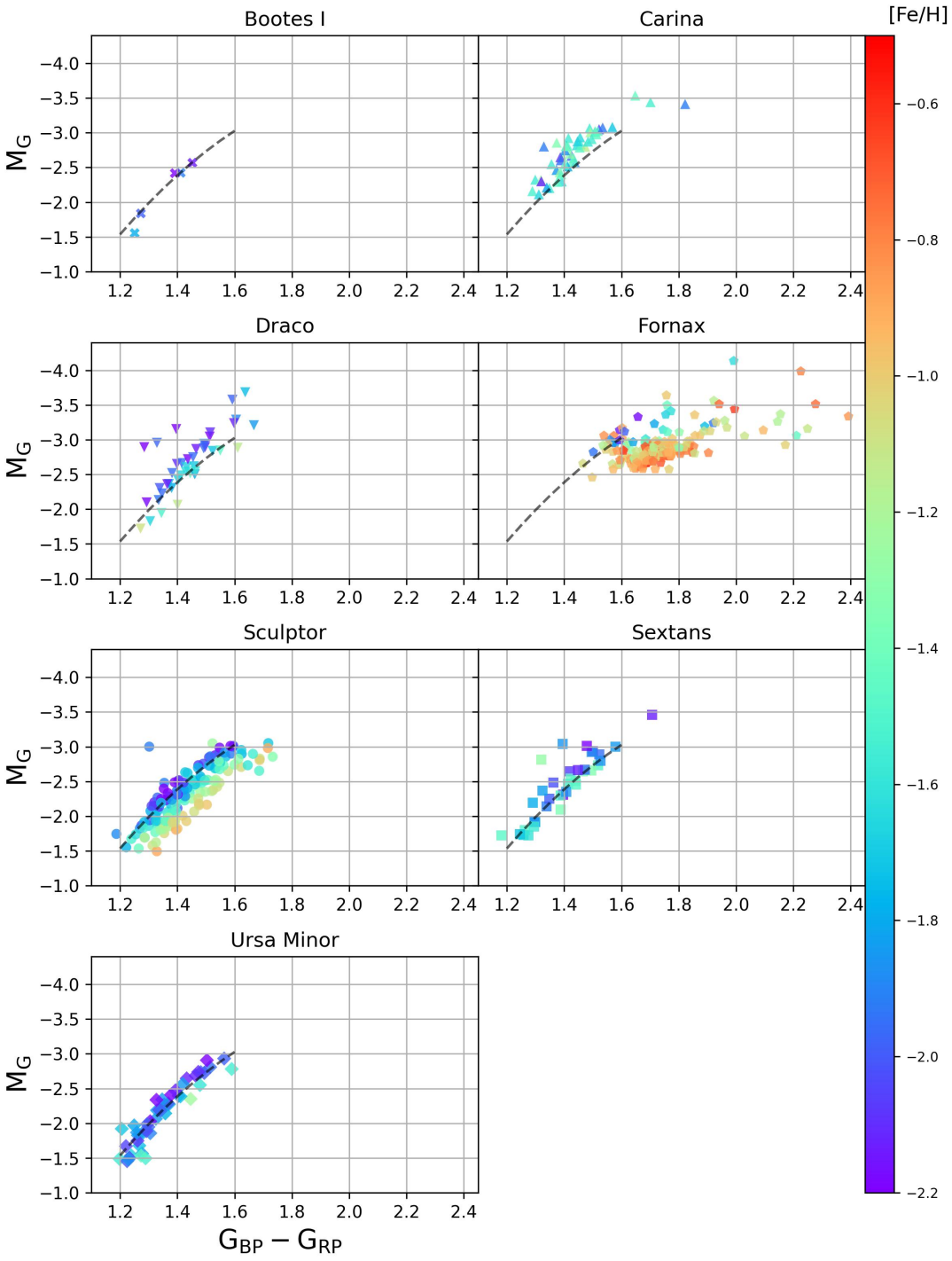

Figure 2. Gaia absolute color–magnitude diagrams for each dSph. Points are colored by [Fe/H], as indicated by the color bar at right. In each panel, a fit to Ursa Minor is reproduced (black dashed line).

3. APOGEE Stellar Parameters and Abundances for dSph Stars

Stellar parameters and chemical abundances for APOGEE stars are obtained using the APOGEE Stellar Parameters and Chemical Abundances Pipeline (ASPCAP; A. E. García Pérez et al. 2016). ASPCAP uses an 8D synthetic spectral grid created from MARCS model atmospheres (H. Jönsson et al. 2020) using the `synspec` code (I. Hubeny & T. Lanz 2011) and the line list described in V. V. Smith et al. (2021). The chi-squared minimization code, `FERRE` (C. Allende Prieto et al. 2006), is used to return a best-fit spectrum from this synthetic grid. This synthetic spectral grid only goes as metal-poor as [Fe/H] $= -2.5$, so our abundance analysis of these galaxies is limited to [Fe/H] > -2.5. More details on the version of ASPCAP used in DR17 can be found in Abdurro'uf et al. (2021).

Unlike many other stellar populations explored in APOGEE, the dSphs are metal-poor, with the most metal-rich stars across the literature being [Fe/H] ~ -0.5 for Fornax and [Fe/H] $\lesssim -0.9$ across the other dSphs (but see Y. Yang et al. 2024

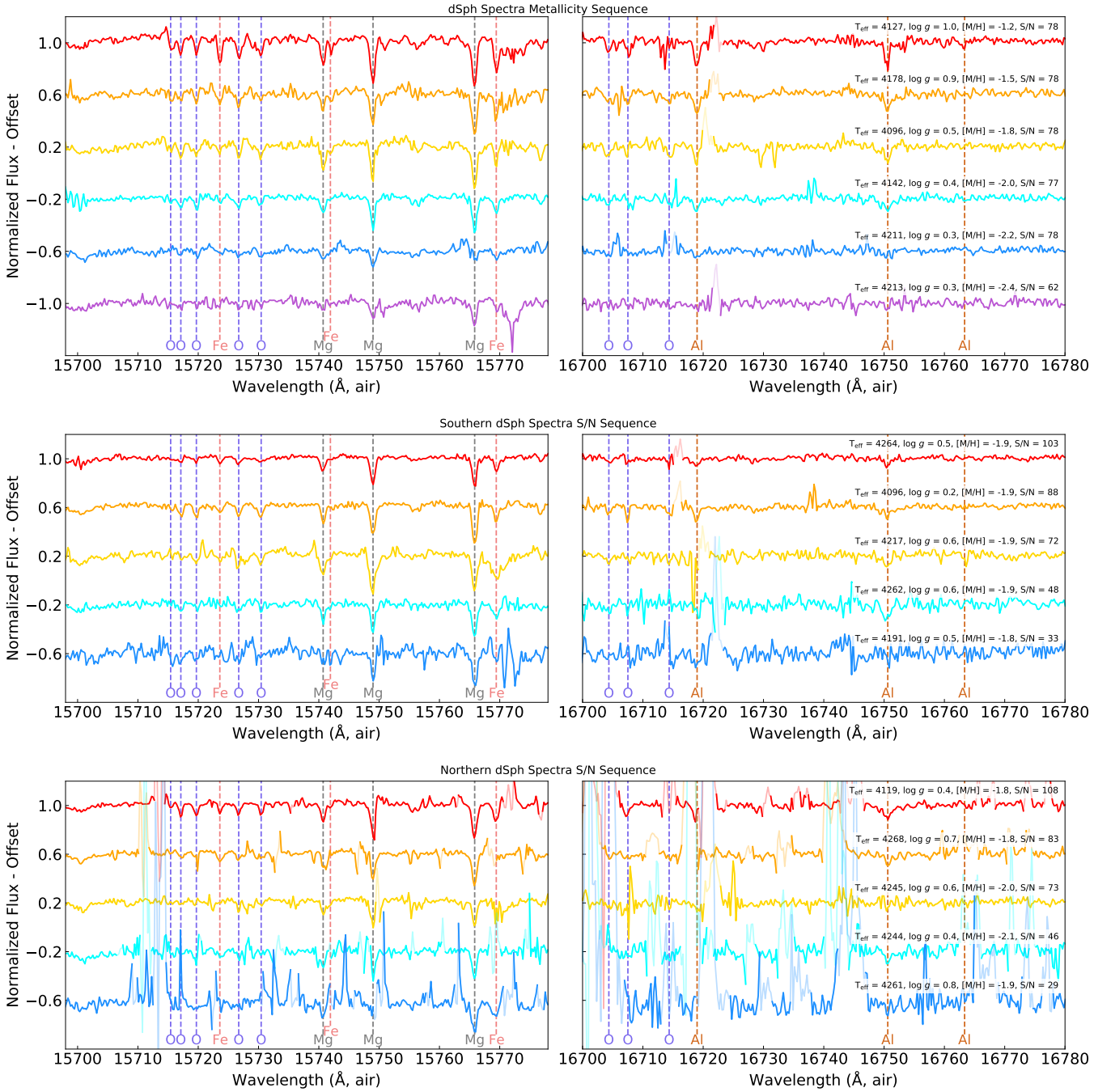

Figure 3. Continuum normalized APOGEE spectra of dSph stars as a function of metallicity (top row), or S/N for stars observed in the south (middle row) and in the north (bottom row). Relatively strong lines are identified in a spectral window around the strong Mg I lines (left panel) and Al I lines (right panel). Lines marked as O indicate OH features. Pixels with uncertainties >25% are masked as transparent for clarity. In the top row, stars with S/N ∼ 70 with $T_{\rm eff}$ ∼ 4550 and log g ∼ 0.5 are compared from [M/H] from −1.2 to −2.4 from top to bottom. In the middle and bottom panel, stars with $T_{\rm eff}$ ∼ 4550 and log g ∼ 0.5 are compared with S/N 100 to 30 from top to bottom.

for signs of a small handful of more metal-rich stars in, e.g., Sculptor). Although considerable work has been undertaken to understand the precision and accuracy of the APOGEE measurements, these works typically focus on stars in the solar neighborhood for which the abundances are within ±0.5 dex of solar and stretching to [Fe/H] ∼ −1.0 at the extremes (see, e.g., H. Jönsson et al. 2018, 2020, among others). An exception to this is the work on globular clusters, e.g., D. Geisler et al. (2021) and D. L. Nidever et al. (2020). Moreover, these works generally focus on the most robust results from high-S/N spectra (S/N ∼100 per pixel); for context, the mean magnitude of the dSph members is $H = 14.8$, which is 1 magnitude fainter than the S/N ∼ 100 magnitude limit for a 24 hr plate. Thus, before we use the measurements for the dSphs, we must explore the APOGEE spectral quality at lower S/N and understand the ASPCAP performance for low-metallicity stars. In Section 3.1 we show some dSph spectra and discuss the obvious limitations of the data, and in Section 3.2 we describe our prescription for upper limits on the APOGEE abundance measurements of these low-metallicity, low-S/N spectra.

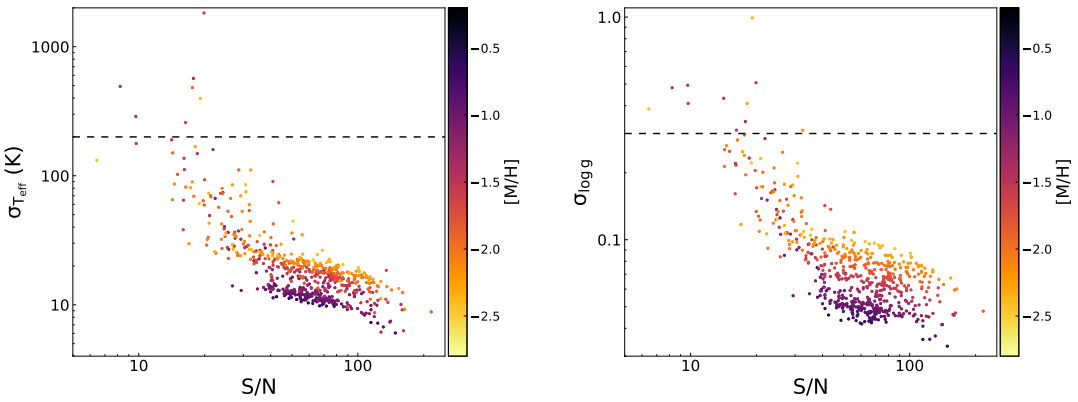

Figure 4. The $T_{\rm eff}$ and $\log g$ errors from ASPCAP are a complicated function of spectral S/N (as measured by SNREV) and the overall metallicity ([M/H]). We exclude stars with errors greater than these by removing those with errors greater than 200 K and 0.3 in $T_{\rm eff}$ and $\log g$, respectively (indicated by dashed lines). This is because these stars have parameters that are too uncertain to provide usable information.

3.1. APOGEE dSph Data Quality and Abundance Uncertainties

Figure 3 shows example APOGEE spectra for dSph members in spectral windows around the strongest Mg I and Al I lines. These spectra were selected to highlight two of the challenges APOGEE faces in measuring stellar parameters and chemical abundances for dSph stars: the low metallicity of the stars, which makes many lines extremely weak, and the low S/N of their spectra, which often makes those weak lines indistinguishable from noise.

In the top panel of Figure 3, we show a sequence of dSph star spectra with $T_{\rm eff} \sim 4550$, $\log g \sim 0.5$, and S/N ~ 70 for a series of metallicities, [M/H] from -1.2 (top spectrum, red) to -2.4 (bottom spectrum, purple). The vertical lines indicate the wavelength for OH, Fe I, and Mg I (left) and OH and Al I (right). The Mg I and Al I features, in particular, are among the strongest lines in the APOGEE spectral range. This illustrates that at the lowest metallicities that APOGEE can measure ([Fe/H] $= -2.5$, which is the low-metallicity edge of the synthetic spectral grid), even the strongest spectral features can grow weak or disappear entirely. This effectively limits the number of elements that APOGEE is able to accurately measure at the lowest metallicities to only the elements with the strongest lines or those species with strong enhancements. dSph spectra taken with APOGEE-N tend to be of lower quality than with APOGEE-S, even at fixed reported S/N; thus, defining reliable measurements for the full sample means that a global S/N restriction to the dataset of interest, as is commonly used in other works using APOGEE data, will not result in a uniform quality to any measured quantities, either stellar parameters or abundances.

Figure 3 shows that there are many measurable features in the APOGEE spectra of dwarf galaxies, but a simple S/N threshold is not enough to select "reliable" measurements. Rather than creating criteria that separate reliable from bad measurements, we derive theoretical upper limits, as described in detail in Section 3.2. We first make use of some of the APOGEE quality flags and uncertainties to remove stars with probably bad parameters/abundances from our sample.

To begin with, we remove any stars that have the ASPCAPFLAG quality flag STAR_BAD set, as this indicates that the outputs from ASPCAP are suspect. We also remove any stars that lie near the ASPCAP metallicity grid edge with [M/H] < -2.4 or near the high edge of the carbon grid with [C/M] > 0.9; in either case, the stars are likely not well modeled, since they may have parameters beyond these grid edges.

Second, we remove stars that have large reported ASPCAP uncertainties. Figure 4 shows how the ASPCAP uncertainties in $T_{\rm eff}$ ($\sigma_{T\rm eff}$) (left) and in $\log g$($\sigma_{\log g}$) (right) are complex functions of S/N and overall metallicity ([M/H]). We remove stars with the poorest quality by removing those with errors greater than $\sigma_{T\rm eff} > 200$ K and $\sigma_{\log g} > 0.3$, which are indicated by dashed lines in Figure 4. In addition we remove a sample of stars that have calibrated ASPCAP stellar parameters outside of reasonable ranges for luminous red giants that we would observe in relatively old, metal-poor systems at these distances. Examples of these stellar parameters are ones that are very hot, putting these stars as B, A, or F type stars (often because their low metallicity and S/Ns are consistent with featureless spectra), or stars that ASPCAP assigns as dwarfs. Some of these appear to be variable or carbon stars, which ASPCAP likely has not modeled correctly. These stars and the rationale for rejection are given in Appendix A.2.

3.2. Abundance Upper Limits

Much of the vetting of the APOGEE stellar parameters and abundances, to date, has focused on the high-S/N regime, e.g., S/N $\gtrsim$ 100, and/or stars of high to moderate metallicity, which is appropriate for the bulk of the APOGEE main red star sample (e.g., G. Zasowski et al. 2013). During DR17 calibration, we placed restrictions on which ASPCAP results were considered "reliable" based on the effective temperature ($T_{\rm eff}$) and $\log g$ of the star, e.g., limiting the $T_{\rm eff}$ ranges in which abundances of a given element are reported because suspect $T_{\rm eff}$ trends suggest that lines are severely blended or simply not detectable at typical APOGEE S/N $\gtrsim$ 100. Although the dSph stars are generally within the normal $T_{\rm eff}$ and $\log g$ range for most species to be reliably measurable at solar abundances (and thus are reported by ASCPAP), the stars are at both significantly lower metallicity and lower S/N than a typical APOGEE star, so APOGEE's lack of abundance upper-limit treatment means that unmeasurable abundances may be reported for certain elements. In this section, we describe our procedure to determine when a measurement reported in the APOGEE catalog is actually measurable at a given S/N and $T_{\rm eff}$.

Many abundance determinations use a line-by-line approach, but APOGEE spectral fitting is a full-spectrum approach that isolates individual species using windowing functions and fitting all features simultaneously. In a line-by-line approach, the abundance detection limit can be determined in its simplest fashion using the depth of the line at a given $T_{\rm eff}$ compared to the S/N of a typical spectrum (see, e.g., C. R. Hayes et al. 2022). We modify the spirit of this methodology and apply it to the APOGEE methods. The method is fully described, with an exemplar element (Ca), in Appendix B, but we briefly describe it here.

For a given element, we produce synthetic spectra at a range of temperatures and abundances of that element. By comparison of these syntheses to synthetic spectra without the lines of that element, we can measure the line depth of this element alone. Using the pixel weights from the elemental windows that APOGEE uses to derive abundances, we measure a weighted-average line depth, $D_{\rm wavg}$, that is determined across all lines with nonzero window weights for that element at each temperature and abundance. In noisy observations, the spectral noise per pixel ($\sigma_{\rm pix}$) averaged over the weighted number of pixels ($N_{\rm wavg}$) is $\sigma_{\rm wavg} = \sigma_{\rm pix}/\sqrt{N_{\rm wavg}}$. We can therefore set a noise threshold according to $D_{\rm wavg} > \chi \cdot \sigma_{\rm wavg}$, where we have chosen $\chi = 4.0$; i.e., for an element to be detectable, we require the weighted-average line depth to be 4.0 times larger than the noise on that measurement. This threshold was chosen based on visual inspection of the spectra of stars near the detection limits and comparison with the abundance measurements from V. Hill et al. (2019), when possible.

Because the spectral noise (of normalized spectra) is $\sigma_{\rm pix} = 1/({\rm S/N})$, this is equivalent to setting a threshold S/N, below which we would not be able to measure that element in the synthetic spectrum: ${\rm S/N_{limit}} = \chi/(D_{\rm wavg}\sqrt{N_{\rm wavg}})$. We calculate these S/N limits for our range of synthesized temperatures and abundances. This combination of temperatures, abundances, and the S/N thresholds then allows us to parameterize the detection threshold for each element.

Instead of deriving a relation to calculate the S/N threshold as a function of temperature and abundance, however, it is more useful to produce a relationship that defines the upper limit on abundances as a function of temperature and S/N. By doing so, we can provide abundance upper limits for stars that are below our detection threshold. So, we fit a function of the form:

$$[{\rm X/H}]_{\rm limit} = \alpha + \beta\left(\frac{T_{\rm eff}}{1000\ {\rm K}}\right) + \gamma\log_{10}({\rm S/N}) + \delta[(\log_{10}({\rm S/N}))]^2\,, \quad (1)$$

to the distributions of $T_{\rm eff}$, [X/H], and S/N threshold values from our synthetic spectra, to determine the optimal coefficients α, β, γ, and δ for our upper-limit threshold relations. The coefficients for 17 elements are given in Table 4. A more detailed account of this process is given in Appendix B.

Using these relations, we then flag any abundances whose [X/H] measurement from APOGEE is within 1σ (using the reported abundance uncertainties) of falling below the upper limit for that star's temperature and S/N. In the subsequent analysis, we will either not show abundances that are considered upper limits in this analysis, or clearly identify them as having upper-limit measurements, where their upper limit is the maximum of the upper-limit relation for that star's temperature and S/N or the APOGEE reported abundance (in the case that the star is within 1σ of the upper-limit relation).

Table 4
Coefficients to Determine Detection Limits for 17 Elements in APOGEE DR17

Species	α	β	γ	δ
C	−5.60	1.40	−1.90	0.209
N	−3.33	1.11	−1.87	0.210
O	−21.61	5.75	−4.76	0.601
Na	−0.80	0.55	−1.12	0.017
Mg	0.38	0.58	−5.17	1.116
Al	−0.18	0.64	−5.09	1.226
Si	0.85	0.33	−4.68	1.078
S	4.66	−0.48	−2.06	0.171
K	−0.68	0.52	−1.57	0.099
V	−4.92	1.50	−1.09	0.012
Ca	−1.32	0.59	−1.57	0.108
Cr	−1.45	0.67	−1.31	0.050
Mn	−1.61	0.61	−1.85	0.188
Co	−2.69	0.89	−1.32	0.058
Fe	−1.88	0.44	−1.91	0.273
Ni	−0.68	0.43	−1.78	0.160
Ce	−0.93	0.51	−1.84	0.174

One important caveat about our methodology is that, near the 4σ detection threshold, we can potentially get a few remaining false-positive detections of stars with very high [X/Fe] abundance ratios, i.e., the reported APOGEE abundance would suggest it should be detectable, but visible inspection shows that these high abundances are merely a result of large, local noise in the spectra, e.g., poor sky-subtraction or telluric corrections. Thus, our methodology is sensitive to some high abundance false positives.

Detailed notes on individual elements can be found in Appendix B, but based on this upper-limit analysis, we exclude the Na, S, and V abundances from this work. We also remove 25 stars that should not have measurable [Fe/H] and 12 stars that should not have measurable [Mg/Fe], as suggested by the upper-limit analysis.

3.3. Final Dwarf Galaxy Giant Sample

Of the 731 stars that we determined to be members of dSphs, 181 are removed for the various reasons listed above and summarized here:

1. Star bad.
2. Grid edge in [M/H] and [C/M].
3. ASPCAP uncertainty.
4. Unreasonable ASPCAP parameters (e.g., log$g$ values consistent with main-sequence stars that would be much too faint to be observed by APOGEE if they were actually in the dSphs).
5. Beyond theoretical upper limits.

Approximately 50 stars were targeted as dSph members based on literature results that are not included in our final membership sample. Most of the spectra had poor overall data quality (SNREV< 34), but for ∼12, we provide further notes in Appendix A.2. The final APOGEE dSph sample with measurable chemical abundances consists of 518 stars across the seven galaxies that have reliable measurements of at least [Fe/H] and [Mg/Fe]. For the other elements, we show in

Table 5
Final Chemistry Sample with True Measurements in APOGEE DR17

Species	Fornax	Sculptor	Carina	Ursa Minor	Draco	Sextans	Bootes
C	195	34	20	4	4	1	0
N	190	27	12	2	3	0	0
O	208	112	41	27	38	19	3
Na	0 (2)	0	0	0	0 (1)	0	0
Mg	207	145	49	41	41	32	3
Al	191	99	40	19	21	14	0
Si	208	146	50	43	42	32	5
S	0 (32)	0 (3)	0 (2)	0	0	0	0
K	79	1	0	0	0	0	0
Ca	169	19	4	1	2	0	0
V	4(6)	0	0	0	0	0	0
Cr	33	2	0	0	0	0	0
Mn	152	31	17	5	2	1	0
Fe	208	149	50	47	42	36	5
Co	74	3	0	0	0	0	0
Ni	178	29	8	2	3	1	0
Ce	68	4	4	2	0	0	0

Note. For entries with two numbers: () number indicates formal formulaic measurements, and number without () indicates correction for visual inspection.

Table 6
Stellar Abundances Presented in This Work

APOGEE ID	Galaxy	[Fe/H]	[C/Fe]	$[C/Fe]_{lim}$	[Mg/Fe]	$[Mg/Fe]_{lim}$	[Ni/Fe]	$[Ni/Fe]_{lim}$	...
2M13595091+1430029	Bootes 1	−1.92	⋯	−0.1	−0.1	⋯	⋯	0.53	...
2M06405789–5102276	Carina	−1.34	−0.55	⋯	−0.33	⋯	−0.08	⋯	...
2M17185759+5754142	Draco	−2.0	⋯	0.14	0.13	⋯	⋯	⋯	...
2M02393076–3451354	Fornax	−0.94	−0.57	⋯	−0.26	⋯	−0.27	⋯	...
2M00591209–3346208	Sculptor	−1.7	0.2	⋯	0.12	⋯	⋯	0.07	...
2M10135723–0144452	Sextans	−1.5	⋯	−0.4	−0.45	⋯	⋯	0.14	...
2M15043661+6718538	Ursa Minor	−1.8	⋯	0.04	0.03	⋯	⋯	0.55	...
...	...	...	...	...	...	...	...	...	...

Note. A full machine-readable table including all elements presented in this work is available. Also, $[X/Fe]_{lim}$ indicates the measurement is an upper limit.
(This table is available in its entirety in machine-readable form in the online article.)

Table 5 how many stars in each galaxy have measurable abundances after considering the upper limits. Examples of these measurements are presented in Table 6, and a machine-readable table is available.

4. Chemical Abundance Patterns of dSphs in APOGEE

In the subsections to follow, chemical abundance patterns ([X/Fe] for element X) for reliable elements are shown as a function of [Fe/H]. Figure 5 shows C and N, Figure 6 depicts the α elements (O, Mg, Si, and Ca), Figure 7 shows the asymptotic giant branch (AGB) + Ia elements (Al, Mn, Ni, and Ce), and Figure 8 presents other elements (K, S, Cr, and Co). In each of these figures, the data for each chemical abundance are shown in two ways: on the left, individual points are color-coded according to the dSph, and on the right, trend lines are shown for each dSph using the same colors (dashed lines). The symbols and color-coding are as follows: Fornax is magenta and/or pentagons, Sculptor is red and/or circles, Carina is orange and/or upward triangles, Sextans is green and/or squares, Ursa Minor is cyan and/or diamonds, Draco is blue and/or downward triangles, and Bootes I is purple and/or "x" symbols. In the left panels, likely carbon stars are circled, where we define a "carbon star" as a star with [C/O] > 0.27, which, in linear abundances, means that the star has more carbon in its atmosphere than oxygen. These carbon stars may have problematic derived abundances for a number of reasons, including potential variable stars and the rapid changes in the ASPCAP synthetic spectrum grid over the C/O = 1 boundary. In both panels of Figures 5–8, the MW APOGEE comparison samples are shown (see Appendix C for selection details) for the high-α disk (black), the inner galaxy/bulge-like stars (gray), the low-α disk (pink), and the GSE+inner halo (dark pink). In both panels, the approximate grid edge is shown as the dotted black line, and the approximate grid point before the edge shown as the gray dotted line; these are approximate because the calibration of the abundances is performed in such a way that individual sources can move across these boundaries (see the calibration discussions in H. Jönsson et al. 2020; Holtzman et al. 2025, in preparation).

The trend lines shown in the right panels of Figures 5–8 are made using an LOWESS (locally weighted scatterplot smoothing) algorithm. The upper-limit analysis (Equation (1) and Appendix B) can bias the determination of these trend lines if a large fraction of the sample is removed. We indicate this by reducing the opacity of the lines when more than 50% of the sample below a given [Fe/H] is removed due to the upper limits; we plot these to give the reader a sense of the apparent trends, as we still have some abundance information at these metallicities, but also to convey that these apparent trends are less clear. In some cases, we may be able to recover constraints on these trends using the upper limits, but we do not attempt that here.

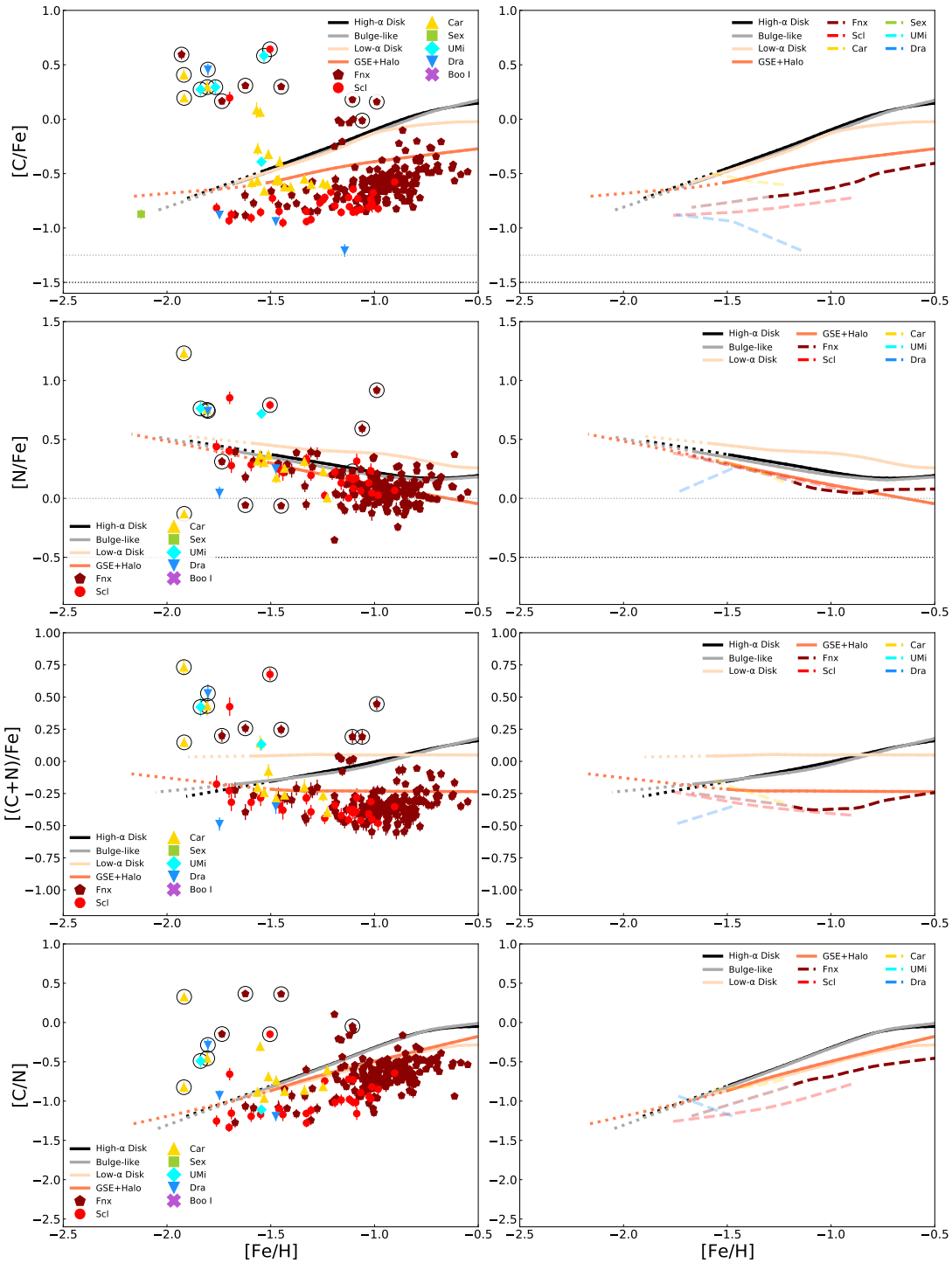

Figure 5. The APOGEE [C/Fe], [N/Fe], [(C+N)/Fe], and [C/N] are shown as a function of metallicity for stars with good abundances in each dSph galaxy (i.e., not identified as upper limits and having uncertainties <0.3 dex). The left panels show the abundances of individual stars (Fornax—dark red pentagons, Sculptor—red circles, Sextans—orange squares, Carina—yellow triangles, Ursa Minor—cyan diamonds, Draco—blue downward triangles, Bootes I—purple crosses) in comparison to LOWESS smoothed distributions of four MW comparison samples (high-α disk—black line, low-α disk—gray, the bulge-like sample—brown, low-α halo—light brown). In the right panels, we show the equivalent LOWESS smoothed abundance distributions for each of the dSphs (dashed lines with the same color-coding), and are transparent at metallicities below which more than half of the abundance measurements are considered bad for that galaxy. Potential carbon stars are also identified (points surrounded by a black circle).

4.1. C, N, C+N, and C/N

Figure 5 shows the APOGEE, [C/Fe], [N/Fe], [(C+N)/Fe], and [C/N] (from top to bottom) as a function of metallicity [Fe/H] for each galaxy. APOGEE provides carbon and nitrogen abundances determined from (1) the entire spectrum, which we refer to as the parameter-level abundances (because these are fit simultaneously with other stellar parameters) and (2) selected windows around C and N sensitive features. We use the parameter-level fits for our analysis, but find that the windowed [C/Fe] and [N/Fe] abundances do track the

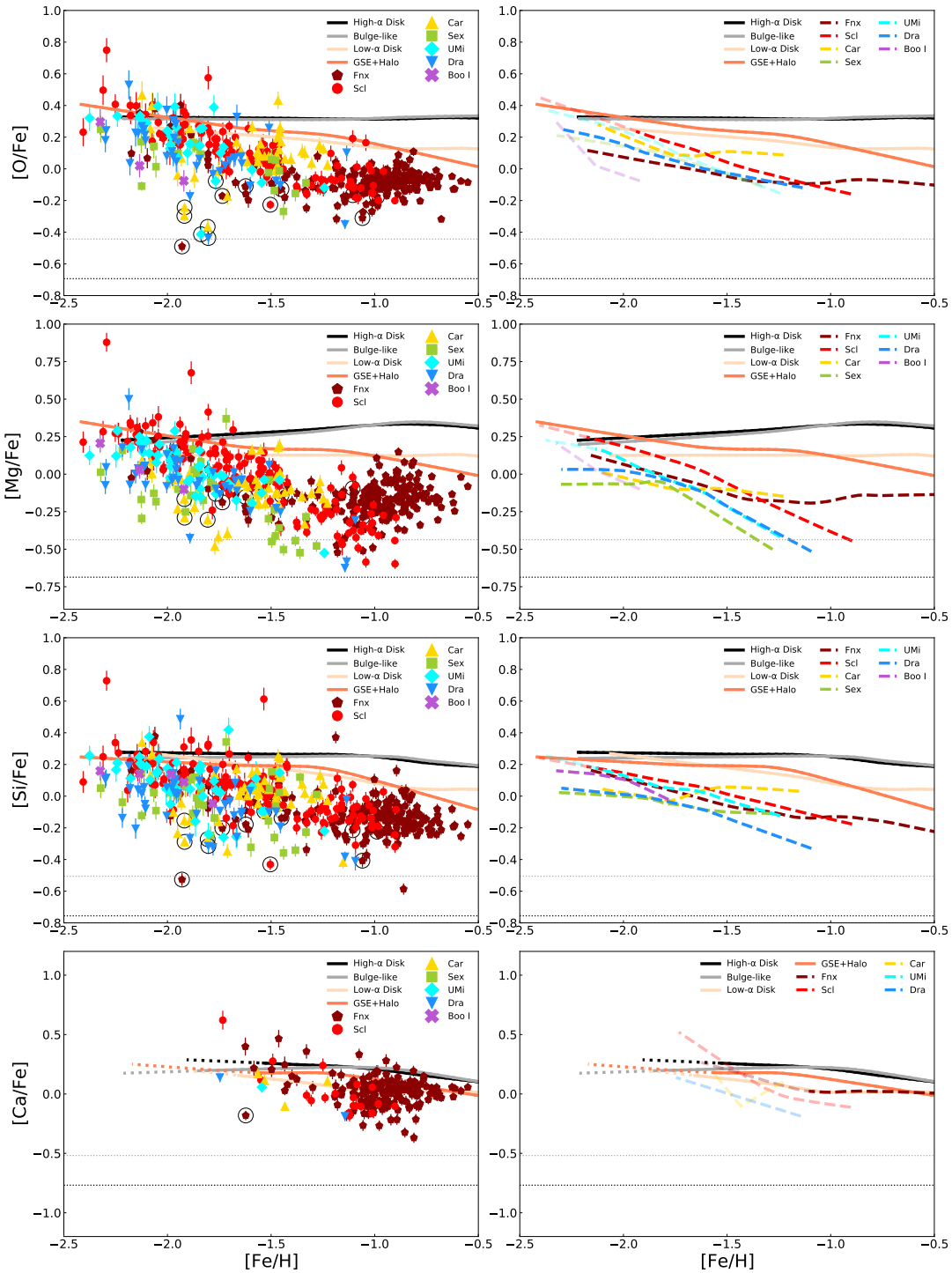

Figure 6. The APOGEE [X/Fe] abundance ratios for O, Mg, Si, and Ca vs. metallicity for stars (left panels) with good abundance measurements in each dSph galaxy and the abundance trends (right panels) of each dSph (as shown in Figure 5).

parameter-level abundances relatively well in the dSph sample (with a slight bias in the windowed abundances +0.022 above the parameter-level fits for C, and −0.003 for N), though the errors on the windowed [C/Fe] abundances are slightly larger.

[C/Fe]. The decline in [C/Fe] with decreasing [Fe/H] across all galaxies, including the MW, shown in the top row of Figure 5 is consistent with increased efficiency of extra mixing in red giant stars, as described in R. G. Gratton et al. (2000). At metallicities [Fe/H] > -1.5, there are some tentative differences between the C abundances of several dSphs, as best seen in the trend lines of the top-right panel of Figure 5. For example, there appear to be ∼0.5 dex differences in the mean [C/Fe] abundance between Carina (yellow) and Draco (blue), with Sculptor (red) and Fornax (magenta) between. At [Fe/H] ~ -1, there is a ∼0.2 dex offset between the [C/Fe] abundances of Sculptor and Fornax. At any given metallicity, the dSph stars may have different ages, so these differences in C could be due to differences in mass-dependent internal mixing as stars ascend the red giant branch, or they could reflect underlying chemical evolution differences in the dSphs. In addition, the Fornax and

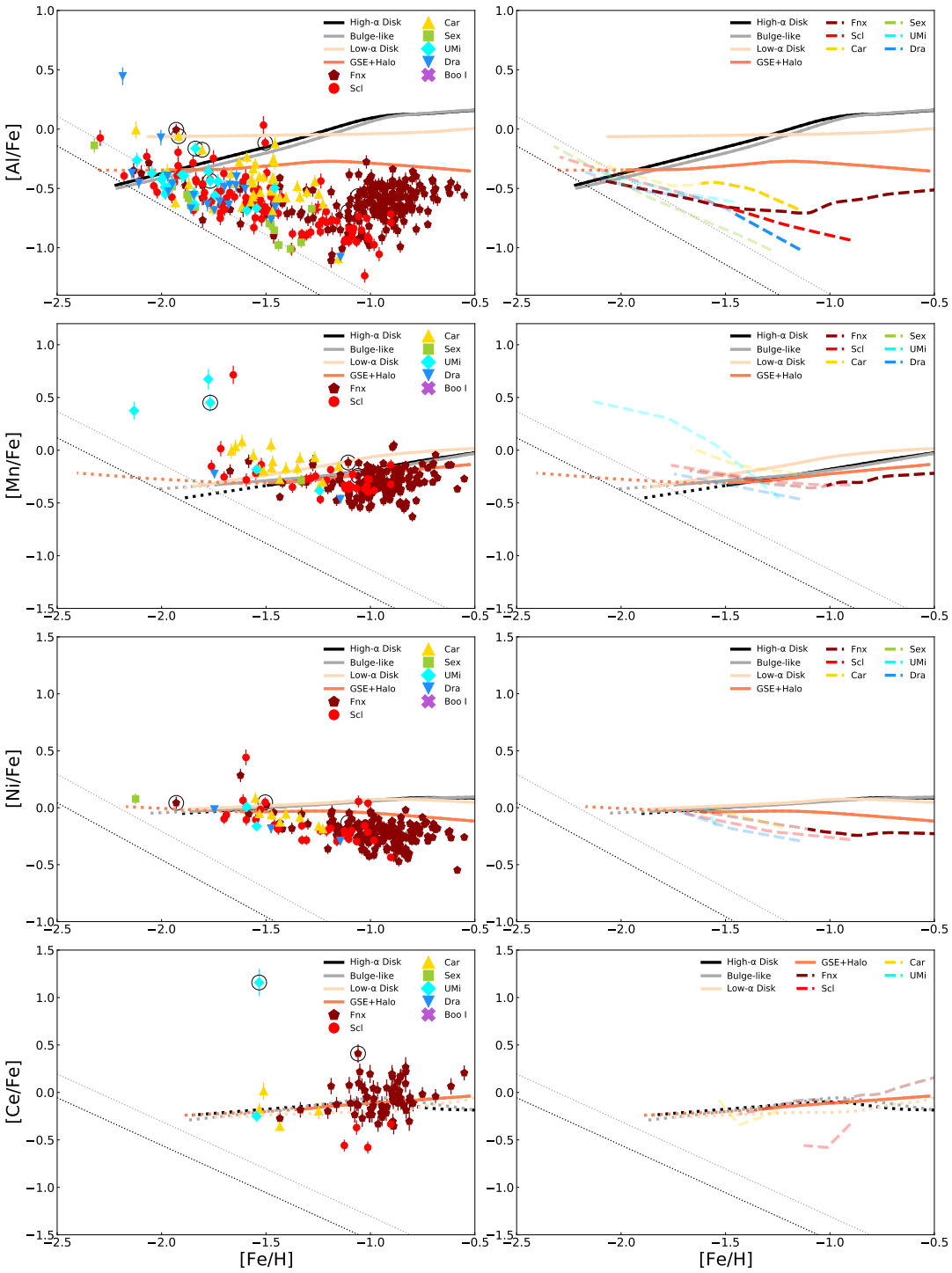

Figure 7. The APOGEE [X/Fe] abundance ratios for Al, Mn, Ni, and Ce vs. metallicity for stars (left panels) with good abundance measurements in each dSph galaxy and the abundance trends (right panels) of each dSph (as shown in Figure 5).

Sculptor samples near [Fe/H] ~ -1 have different mean surface gravities, with the Fornax sample having log(g) $\sim$0.7 dex, while the Sculptor sample has log(g) $\sim$ 1.2. This could point toward a difference between more-massive AGB star abundances in Fornax and lower-mass red giant abundances in Sculptor, although systemic biases in the analysis as a function of log(g) also cannot be ruled out. The MW sample is weighted toward stars of higher surface gravity, which likely weights the C abundance toward higher carbon abundances, although mass/age differences also cannot be ruled out.

Among the Fornax population, 20 stars have [C/Fe] > -0.1, and of these, 16 are either above the RGB tip or 0.1 dex bluer in $G_{BP} - G_{RP}$ than the bulk of the stars at their metallicities. These stars are likely AGB stars, and the anonymously high [C/Fe] probably reflects a stellar evolutionary increase and not a galactic chemical evolution. However, not all AGB stars show enhanced [C/Fe], e.g., oxygen-rich asymptotic giant branch (O-AGB) stars. Below the TRGB, some of the higher C abundance stars could be AGB stars since AGB stars can be metal-poor C-enhanced stars, metal-poor C-normal stars, and metal-rich

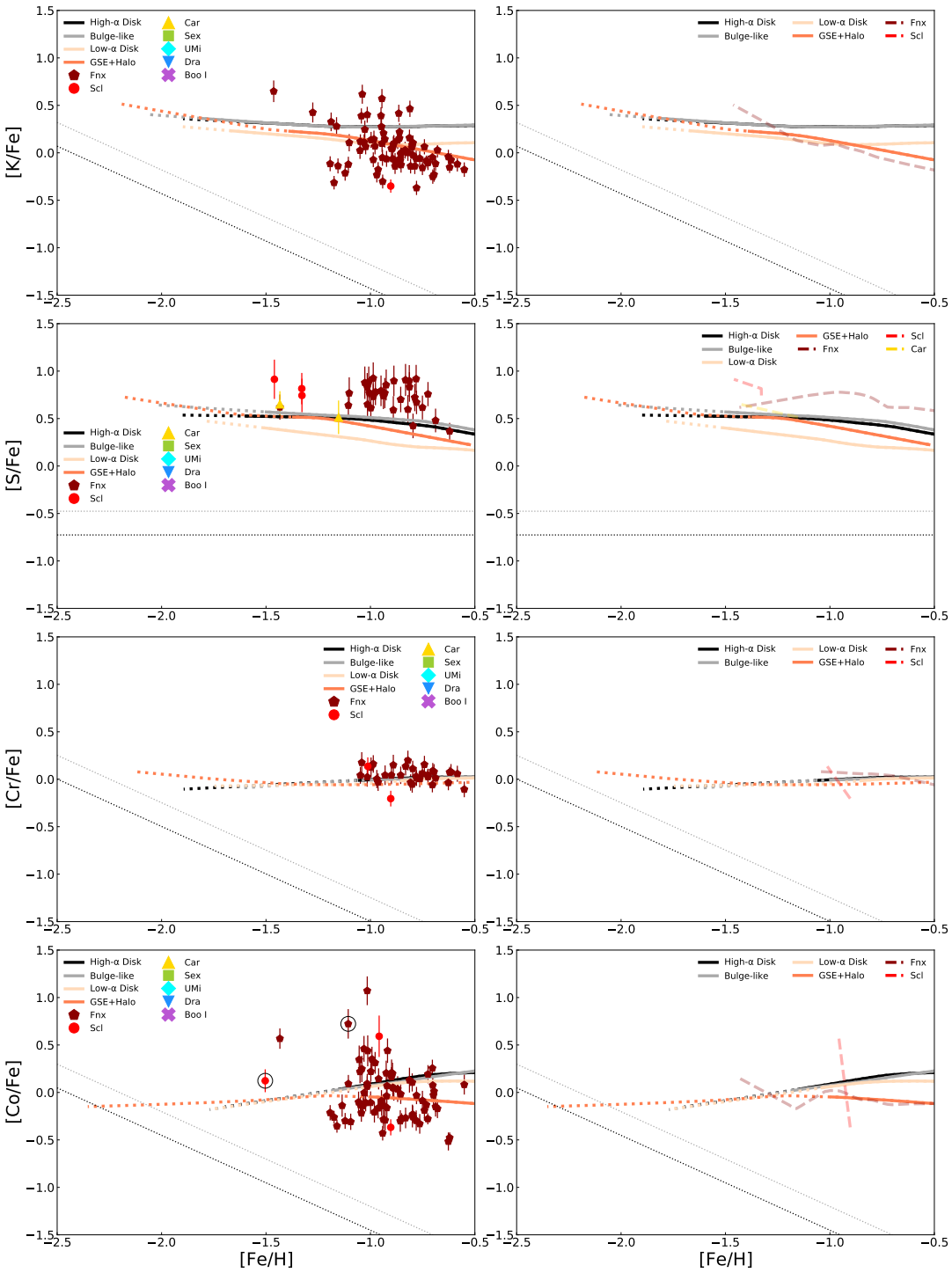

Figure 8. The APOGEE [X/Fe] abundance ratios for K, V, Cr, and Co vs. metallicity for stars (left panels) with good abundance measurements in each dSph galaxy and the abundance trends (right panels) of each dSph (as shown in Figure 5).

stars C-normal stars, or they could be RGB stars with a mass transfer signature from a binary companion.

[N/Fe]. In the *H* band, the only source of nitrogen abundances comes from the CN molecule. For this reason, the carbon abundance must be known independently from the nitrogen abundance. To determine which stars have detectable nitrogen abundances, we require that the star have no carbon and nitrogen upper limits. The N abundance patterns in the dSphs look quite similar to each other, and to the GSE+halo abundance pattern. The low-α "thin" disk appears to be elevated by $\sim$0.5 dex in [N/Fe] relative to the dSphs and MW halo, likely due to the fact that the low-α thin disk is composed of higher-mass giant branch stars that dredged up more N when they ascended the red giant branch as compared to the lower mass, and therefore, older giants in the dSphs and MW halo.

[(C+N)/Fe]. To attempt to separate out chemical evolution effects from stellar evolution effects on the abundances of C and N, we consider the sum total of these abundances, as first dredge up, to first order, enhances nitrogen and depletes

carbon. In the Fornax and Sculptor datasets, there is an indication for lower [(C+N)/Fe] than all of the Milky Way samples with increasing metallicity. This is likely because the dSphs formed stars with a higher Type Ia/Type II SNe ratio than the MW, resulting in enhanced Fe relative to C+N. Indeed (and as seen in the past in these dSphs) when considering the α-element abundance patterns, we can see that these patterns are also lower than the MW samples, suggesting the more significant influence of Type Ia SNe and their Fe-peak abundance contributions. The most metal-rich Fornax giants show a rise in the [(C+N)/Fe]. As observed by S. Hasselquist et al. (2021) this increase in [(C+N)/Fe] could either be due to a burst of star formation that appears to have altered the abundances of other elements (particularly the α-elements), or because the most metal-rich Fornax stars are relatively young (F. Pont et al. 2004; E. N. Kirby et al. 2010; B. Letarte et al. 2010; B. Lemasle et al. 2014), and this increase is instead due to contributions from AGB stars.

[C/N]. The [C/N] abundance of a red giant star can be indicative of its mass, at least at higher metallicity. It is not clear how reliable of a mass indicator the [C/N] abundance is at lower metallicity, where extra mixing apparently plays a role. However, in the bottom row of Figure 5, we find that Sculptor and Fornax both exhibit [C/N] abundances that fall below the MW trend. For Sculptor, Carina, Draco, and Ursa Minor, >50% of the sample is removed for upper limits over the entire metallicity range. This means that interpretation of any offsets in the [C/N] between these galaxies should be treated with a high degree of skepticism. For example, the Carina [C/N] points fall above the Sculptor points, while the [(C+N)/Fe] distributions are very similar, which, if interpreted as being due to mass/age, would imply that the Carina sample is older than the Sculptor sample at the metallicity over which they overlap. However, this is not what is expected; Carina, particularly the burst stars, should be younger (D. R. Weisz et al. 2014b). We attribute this inconsistency to ab initio higher C abundances and corresponding lower N abundances, or systemics introduced by the large number of upper limits skewing the results.

However, for the metal-rich Fornax stars, the detections outnumber the upper limits. So, if we interpret [C/N] solely as a mass indicator, these abundances would suggest that the metal-rich Fornax stars are more massive than the MW disk stars. Because mass is correlated with age on the giant branch, we can conclude that Fornax has relatively recently formed stars, consistent with the starburst prediction of B. Hendricks et al. (2014) and S. Hasselquist et al. (2021), with the caveats of metallicity and luminosity-dependent extra mixing and evolutionary history.

4.2. The Alpha Elements

Figure 6 shows O, Mg, Si, and Ca following the style established in Figure 5. All together, the dSphs tend to have decreasing [α/Fe] ratios with increasing metallicity, though this pattern flattens at solar or near-solar [α/Fe] for a few galaxies like Carina and Fornax. We can also see that in the trends of each galaxy, this decreasing abundance pattern does have a relative shift among the galaxies. At lower metallicities where all galaxies populate, e.g., [Fe/H] ~ -1.8, we typically see that Scl is the most α-enhanced followed by Draco and Fornax, and then UMi, Car, and Sxt having the lowest α-abundances, and Boo is unclear given how few stars have been observed in it. Although it is not clear whether any of these dwarfs reach an α-abundance plateau and show evidence of an α-knee, it does appear that some of them approach the plateau seen in the MW bulge/thick-disk.

[O/Fe]. O appears to have some of the tightest abundance patterns of the α-elements, though we can see that carbon-enhanced stars appear to have low O abundances. It is unclear if that is because these stars have intrinsically low O abundances, or if because our upper-limit methodology is developed for carbon-normal stars and not carbon-enhanced stars, that perhaps the O in these stars is not easily measurable because the CO lines saturate and the remaining C forms CN molecular features, which masks the *H*-band CO lines.

Although Boo is poorly populated, it does appear to generally be more O-poor on average than other dSphs, which differs from some of the other elements, where these Boo stars seem to have more similar α-element abundances to the other systems.

[Mg/Fe]. Mg is the α-element where we observe the largest differences between each of the galaxies. Examining the distribution of stellar abundances, we can visually see that, at low metallicities, Scl has higher [Mg/Fe] ratios than UMi and Dra, which are again higher than Sxt. Interestingly, we can also see some structure in the chemical abundance patterns of some of these galaxies, particularly Car and Fnx. As shown in S. Hasselquist et al. (2021), in Fornax we see a decreasing [Mg/Fe] abundance pattern with increasing metallicity until [Fe/H] $= -1.2$, where the Fnx [Mg/Fe] abundances begin to increase with increasing [Fe/H]. Similarly in Car, we see a decrease in [Mg/Fe] with increasing [Fe/H] until [Fe/H] $= -1.7$, where we see a $\sim$0.4 dex jump in [Mg/Fe] that is reminiscent of what has been seen in the literature for Car, though perhaps with higher precision here. This feature is washed out in the trend lines because of the small number of stars and the rapid change. As will be discussed in Section 6, these are both consistent with what one would expect if these galaxies experienced a burst of star formation that momentarily increases the number of core collapse SNe and drives the [α/Fe] ratios closer toward pure CCSNe yields. At [Fe/H] ~ -1.1, we find that the Scl [Mg/Fe] abundances are 0.2–0.3 dex lower than the Fornax [Mg/Fe] abundances, but this deficiency is not shared by the other α elements. This could be explained if Mg is the only "pure" Type II SNe α element. The larger ratio of Type Ia/Type II SNe in Sculptor at these metallicities could explain this difference in Mg, if there is an initial mass function (IMF) difference between the two galaxies, or there are metallicity-dependent yields and some delays incorporating SN material into the next generation of stars in one of the two galaxies (e.g., E. N. Kirby et al. 2019; M. A. C. de los Reyes et al. 2022).

[Si/Fe]. Si shows distributions very similar to those of O and Mg, with a potentially larger spread within each system (particularly UMi and Draco). There is also a less pronounced increase in Fnx's [Si/Fe] ratios at high metallicities compared to Mg and O, perhaps because more Si is produced in larger relative quantities in Ia SNe. At [Fe/H] ~ -1.5 to -1, Scl looks flatter than it does in Mg, suggesting an interesting difference in the [Mg/Si] ratios, which appear to differ from those seen in Fnx at the same metallicities.

[Ca/Fe]. Of all of the α-elements investigated in this study, Ca is the most affected by upper limits. Only the highest-metallicity stars have measurable Ca, where we see that it

appears similar to what is seen in some of the other α-elements. For instance, like in O and Si, the highest-metallicity stars in Scl have [Ca/Fe] ratios similar to those of Fnx (unlike in Mg), both of which sit around the solar ratio. The Fnx stars with [Fe/H] > -1.0 have [Ca/Fe] abundance ratios similar to those of the MW low-α disk stars.

4.3. Other Elements

Figure 7 shows Al, Mn, Ni, and Ce following the style established in Figure 5.

[Al/Fe]. Strong lines of Al I appear in the APOGEE spectra, but unfortunately, the APSCAP methodology limits the Al measurements to [Al/H] > -2.5 (the [M/H] grid edge). The significantly subsolar [Al/Fe] ratios seen in the dSphs mean that Al runs into the APOGEE grid edge more quickly than other elements. Therefore, while Al is not significantly affected by the upper-limit cases because of the weakness of the lines, it is limited by the grid edge. The LOWESS trend lines represent this limitation by cutting at the metal-poor end, when needed, to avoid the grid edge values from playing an overwhelming role in the resulting value, i.e., when more than 50% of the values have [Al/H] grid edge "BAD" values. This should not be confused with the LOWESS trend lines representing when more than 50% of the sample may be impacted by upper limits, represented by becoming transparent (in the case of the dSph curves) and dotted (in the case of the MW samples).

The dwarf galaxies fall below all components of the MW except among the most metal-poor stars. Despite this, we can see some differences between the dSphs. The Carina and Fornax dwarfs show a flattening or rising trend in [Al/Fe] with increasing [Fe/H] in their most metal-rich stars, similar to what was found for the α element Mg for these galaxies. This seems to continue to indicate that these two galaxies may have experienced bursts, and the added production of light elements through CCSNe is raising the Al ratios, mirroring the trends seen in [Mg/Fe] and to a lesser extent [O/Fe] and [Si/Fe]. Traditionally, Al production would be associated with N production, but we do not measure N independently, but only through [(C+N)/Fe]. There do not appear to be strong correlations between [(C+N)/Fe] and [Al/Fe].

Draco, Ursa Minor, Sextans, and Sculptor show decreasing [Al/Fe] values throughout their chemical evolution, with the [Al/Fe] abundances quickly dropping below the trend of GSE +MW Halo at [Fe/H] > -2.0.

[Mn/Fe]. Mn, as an Fe-peak element, appears relatively flat across all of the dSphs across the metallicities, where it is not significantly affected by the upper limits. There may be a slight hint that Car has an [Mn/Fe] enhancement over Scl at similar metallicities, but this is based on only small number statistics, so larger samples would be needed to verify this. Some stars have high [Mn/Fe] ratios ($\gtrsim$0.5); these values lie close to the upper-limit thresholds and may suggest that a higher threshold criterion is needed for Mn.

[Ni/Fe]. The [Ni/Fe] abundances are moderately affected by upper limits such that most stars with [Fe/H] < -1.5 do not have reliable [Ni/Fe] measurements. At this metallicity and above, we find that Carina, Scl, and Fnx all exhibit declining [Ni/Fe] abundances with increasing [Fe/H], which put the abundance trends of these galaxies below those of the MW, similar to Al. The [Ni/Fe]–[Fe/H] trend for Fnx apparently flattens out around [Fe/H] ~ -1.0, the same metallicity at which we observe inflection points for the α elements and Al.

[Ce/Fe]. Although the sample of stars with Ce measurements is small, there are some interesting notes from Ce. For instance, most of the Scl upper limits (not shown) and the few bona fide measurements fall below the Fnx detections at the same metallicities. This would be consistent with the idea that Fnx has had much more extended SFH (S. Hasselquist et al. 2021) than Scl (e.g., M. Bettinelli et al. 2019), and given that Ce is produced primarily in AGB stars through the slow neutron capture process, the longer SFH would allow Fnx to build up more Ce over time than Scl with its short evolution.

Remaining elements. Potassium, sulfur, chromium, and cobalt are shown in Figure 8. K, S, Cr, and Co are measured only in a few stars, primarily in Fnx, because it is the most metal-rich. Although the formula we derive for the upper limits rejects 86% of the sample, the remaining 14% exhibits a large spread in values, and/or the upper limits we compute for the dSph stars fill the same part of parameter space as the detections. Thus, it is difficult to separate out real detections from likely upper limits. Because of the upper-limit thresholds for these elements, we cannot draw any significant conclusions about their abundance patterns in the dwarfs. However, for Fnx, we can see that it is consistent with having solar ratios of [K/Fe] and [Cr/Fe] at its highest metallicities. It may also have solar [Co/Fe], though the large scatter prohibits one to see this clearly. We believe that the [S/Fe] detections are not real and consistent with nondetections, as indicated in Table 5.

5. Comparison with the Literature

Many of these galaxies have been studied previously through high-resolution optical observations, and therefore, there exist chemical abundance measurements of individual stars that can be compared to the APOGEE ones presented here. Previous investigations have indicated that the abundances measured in the NIR, like APOGEE, can show systematic offsets from measurements in the literature; the origins are partially the use of different wavelength ranges that probe different layers of the stellar photosphere where, in the NIR, the NLTE effects are lower (see, e.g., S. A. Korotin et al. 2020; Y. Osorio et al. 2020). Because the APOGEE DR17 abundance methodology attempts to correct for NLTE effects on the NIR Mg lines (see Y. Osorio et al. 2020), and many of the optical samples we compare to assume LTE, we speculate that this could be the source of some of the offsets we observe.

Additionally, systematic offsets between the NIR and optical can also arise from the methodology used to measure the abundances, including the synthesis code used, model atmospheres adopted, and assumptions about/fixing of stellar parameters. As an additional caveat, the APOGEE dataset is calibrated to stars near the Sun, so zero-point offsets have been applied to the initial ASPCAP outputs, which might result in systematic differences with optical studies, especially at lower metallicities.

Thus, before comparing the APOGEE results with those in the literature, we first use the literature studies with substantial overlap with APOGEE to derive offsets to align those works to the APOGEE abundance scale; we do this in a simple fashion, deriving a global difference that may neglect abundance-dependent offsets. An example of how this is done for Sculptor is shown in Figure 9. The left panel of Figure 9 shows how the V. Hill et al. (2019) [Mg/Fe]–[Fe/H] abundance pattern

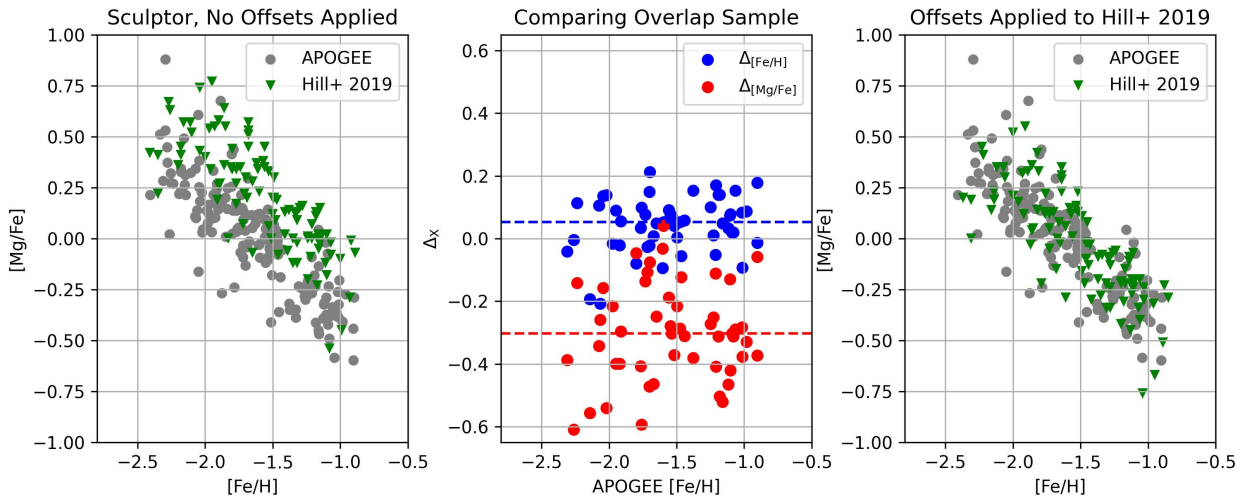

Figure 9. Left panel: the [Mg/Fe]–[Fe/H] abundance patterns of Sculptor for the APOGEE sample in this work (gray circles) and the V. Hill et al. (2019) work (green triangles). While the overall shape is similar between studies, there are clear abundance offsets. Middle panel: offsets in [Fe/H] (blue) and [Mg/Fe] (red) between APOGEE and V. Hill et al. (2019) as a function of APOGEE [Fe/H] for a subset of stars in common between the two studies. Dashed lines mark the median offsets for each abundance. Right panel: similar to the left panel, but with the offsets applied to the V. Hill et al. (2019) demonstrating that, at least for this literature study, the abundances are merely offset from each other and both studies agree on the dependence of [Mg/Fe] on metallicity.

Table 7
Offsets to Place Literature Studies on the APOGEE Scale

Study	Galaxies	N	$\Delta_{[Fe/H]}$	$\sigma_{[Fe/H]}$	$\Delta_{[Mg/H]}$	$\sigma_{[Mg/H]}$	$\Delta_{[Mg/Fe]}$	$\sigma_{[Mg/Fe]}$
J. E. Norris et al. (2010b)	Boo	*	−0.013	0.076	0.353	0.163	0.356	0.165
M. Shetrone et al. (2003)	Car	5	−0.074	0.071	0.203	0.050	0.277	0.104
A. Koch et al. (2008)	Car	6	−0.043	0.130	0.006	0.230	0.043	0.129
B. Lemasle et al. (2012)	Car	17	−0.086	0.099	0.228	0.108	0.314	0.109
K. A. Venn et al. (2012)	Car	4	−0.083	0.089	0.285	0.053	0.353	0.102
J. E. Norris et al. (2017)	Car	13	−0.013	0.076	0.353	0.163	0.356	0.165
M. D. Shetrone et al. (2001)	Dra	4	−0.038	0.058	0.145	0.115	0.183	0.150
J. G. Cohen & W. Huang (2009)	Dra	10	−0.073	0.076	0.111	0.136	0.184	0.086
B. Letarte et al. (2010)	For	28	0.046	0.068	0.075	0.135	0.029	0.124
B. Lemasle et al. (2014)	For	17	−0.086	0.099	0.228	0.108	0.314	0.109
M. Shetrone et al. (2003)	Scl	5	−0.074	0.071	0.203	0.050	0.277	0.104
Á. Skúladóttir et al. (2015)	Scl	42	−0.050	0.084	0.210	0.156	0.271	0.143
V. Hill et al. (2019)	Scl	50	−0.040	0.090	0.260	0.170	0.220	…
M. D. Shetrone et al. (2001)	Sxt	4	−0.038	0.058	0.145	0.115	0.183	0.150
M. D. Shetrone et al. (2001)	UMi	4	−0.038	0.058	0.145	0.115	0.183	0.150
J. G. Cohen & W. Huang (2010)	UMi	10	−0.073	0.076	0.111	0.136	0.184	0.086
U. Ural et al. (2015)	UMi	2	−0.010	…	0.160	…	…	…

compares with what we measure for APOGEE. Although the shape of the sequence is similar between the two studies, there is an apparent offset between them. The middle panel of Figure 9 shows the difference in [Fe/H] and [Mg/Fe] measured between the two studies for a subset of stars observed in both studies. The right panel shows how the two studies compare when global offsets are applied to [Fe/H] and [Mg/Fe] abundances of the V. Hill et al. (2019) data.

We follow a similar approach to each literature sample for each galaxy. The offsets for each study can be found in Table 7, and the results are plotted in Figure 10. The purpose of the following literature comparison is to understand the extent to which any conclusions drawn from APOGEE data can also be drawn from the existing optical data and to determine whether the high-resolution optical data, when added to APOGEE, results in a more complete idea of the SFH of these galaxies. The data in the literature we used for each galaxy are briefly described below. We tried to be as comprehensive as possible, but for several literature sources (because there were no stars with overlap with APOGEE), we were unable to determine an abundance offset.

Bootes. There is no or minimal overlap with APOGEE, so there are no offsets for S. Feltzing et al. (2009), G. Gilmore et al. (2013), M. N. Ishigaki et al. (2014), and A. Frebel et al. (2016). Applied offsets from J. E. Norris et al. (2017) to J. E. Norris et al. (2010b).

Carina. All of the following studies overlap with APOGEE and offsets were derived: B. Lemasle et al. (2012), K. A. Venn et al. (2012), J. E. Norris et al. (2017), A. Koch et al. (2008), and M. Shetrone et al. (2003),

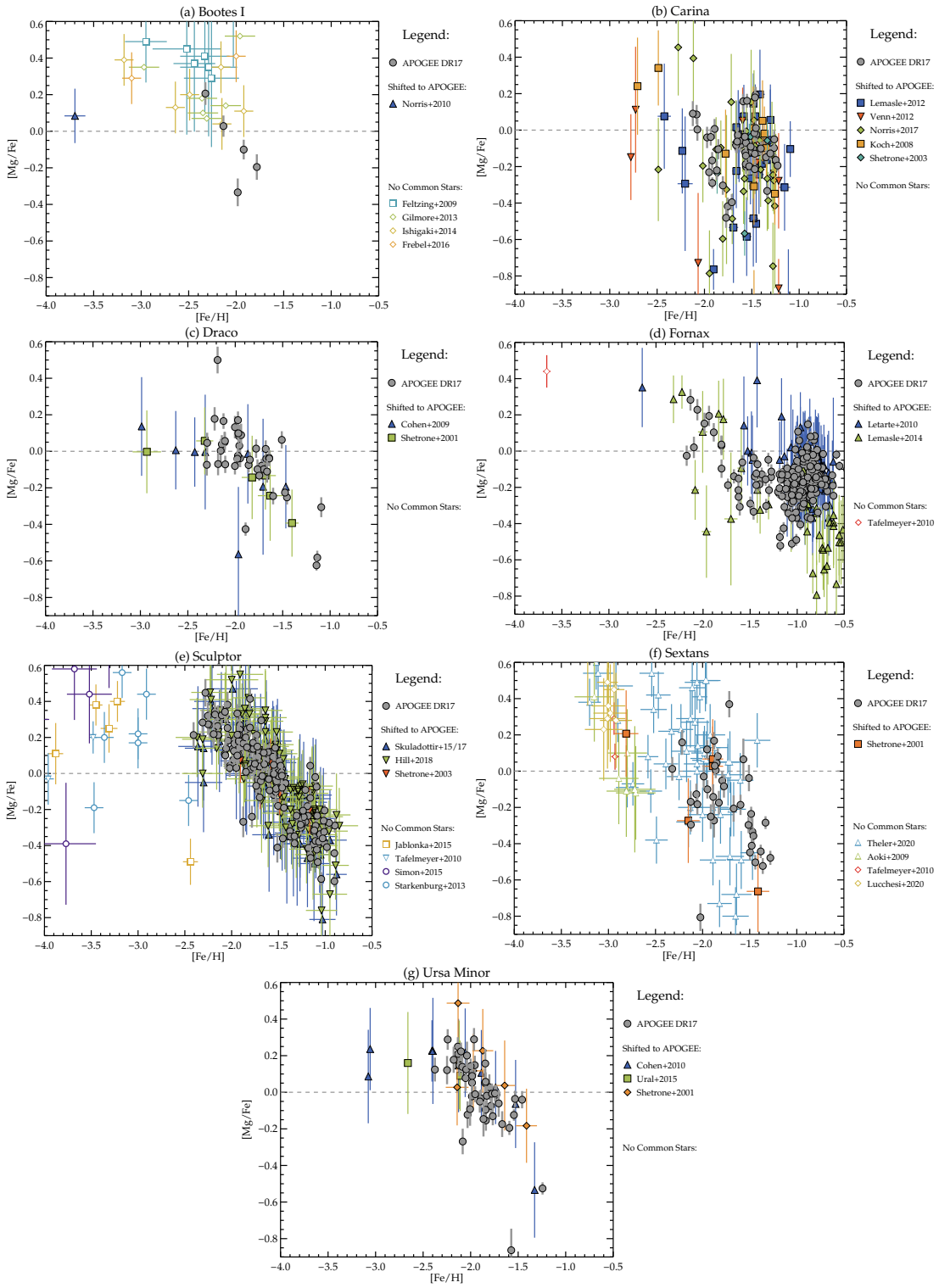

Figure 10. APOGEE sample (gray circles) alongside the literature high-resolution studies. Legends in each panel indicate the studies being shown, and references are provided in Section 5. Open symbols indicate studies presented in the published values, whereas filled symbols indicate studies that have zero-point shifts applied (see Table 7).

Draco. Both J. G. Cohen & W. Huang (2009) and M. D. Shetrone et al. (2001) have enough overlap with APOGEE to determine offsets.

Fornax. Both B. Letarte et al. (2010) and B. Lemasle et al. (2014) have a significant overlap with APOGEE, and the offsets are determined. However, APOGEE did not observe the metal-poor star of M. Tafelmeyer et al. (2010), and it is shown as reported in that study. There was no overlap with the B. Hendricks et al. (2014) study.

Sculptor. The two studies of Á. Skúladóttir et al. (2015, 2017) and V. Hill et al. (2019) both have a significant overlap with the APOGEE sample and are offset to match the APOGEE distribution. We also use offsets for M. Shetrone et al. (2003). However, the studies of P. Jablonka et al. (2015),

M. Tafelmeyer et al. (2010), E. Starkenburg et al. (2013), and J. D. Simon et al. (2015) do not have an overlap sample and are shown as reported.

Sextans. We offset M. D. Shetrone et al. (2001) to the APOGEE scale. However, the studies of M. Tafelmeyer et al. (2010), W. Aoki et al. (2009), R. Theler et al. (2020), and R. Lucchesi et al. (2020) have no overlap observations with APOGEE, and we show them as is.

Ursa Minor. We determined offsets for the studies of J. G. Cohen & W. Huang (2010), U. Ural et al. (2015), and M. D. Shetrone et al. (2001) to place them on the APOGEE scale.

From the literature comparisons in Mg in Figure 10, once zero-points have been applied, we generally see a good agreement between the abundance patterns observed in the literature and those seen here in APOGEE, although depending on the system, the APOGEE measurements are sometimes higher precision, such as in Carina, Sextans, Draco, or Ursa Minor. In other systems like Sculptor, we see that the similar precision literature measurements are (with a zero-point offset) in excellent agreement with APOGEE measurements and find a very similar chemical abundance pattern. For systems like Sculptor, Draco, and Ursa Minor, the combined literature and the APOGEE datasets continue to show relatively simple chemical abundance patterns, where an α-knee might even be visible. It is interesting that the large scatter and unusual chemistry seen in individual literature samples for Carina and Sextans do continue to have an odd chemical abundance distribution with a complex pattern when combining the literature results with zero-points and the higher-precision APOGEE results. In addition, the large scatter seen in Sextans continues to be seen even in the higher-precision APOGEE data, suggesting that this is real, and not entirely due to observational uncertainties.

The one case where we do not see a great agreement between APOGEE and the literature is in Bootes I. However, this is in part due to no overlap between APOGEE and the dominant literature samples, so there may still be zero-point offsets between the two (as there are known to be in Mg; e.g., M. Bergemann et al. 2017; Holtzman et al. 2025, in preparation). This, in addition to the small sample size, makes Bootes I difficult to interpret.

The similarities between APOGEE and the literature, at least in this key APOGEE α-element, give confidence in comparisons between the galaxies across the metallicity range. We discuss some of the basic interpretations of these abundance patterns below. One of the key differences among the dSph abundance patterns is that some show large scatter or complex behavior that is not typically associated with a simple chemical evolution over a short span of metallicity. Examples of systems with increases, jumps, or large scatter at a given metallicity in [α/Fe] are Carina, Fornax, and Sextans, whereas Sculptor, Draco, Ursa Minor, and possibly Bootes I, show monotonically decreasing [α/Fe] with increasing metallicity, with hints of a plateau at low metallicities. The former we interpret as the chemical evolution caused by bursty or periodic star formation that quickly changes the ratio of CCSNe to SN Ia, which can change the α-element and Fe-peak element ratios. The latter have a chemical abundance pattern more indicative of a more constant or quiescent SFH, potentially only experiencing SF at early times in the Universe.

6. Discussion

In principle, the detailed chemical abundances presented here can be used to infer details of the SFH of each dSph. In practice, this is difficult, primarily due to uncertain yield calculations for some elements that result in incorrect chemical evolution models combined with limitations of the spectroscopic abundance themselves, including NLTE. However, in this discussion, we use knowledge of where the elements are generally formed to comment on the SFHs of these galaxies, relating them to general properties of each galaxy such as mass and environment. We begin with the α elements, as they are most easily interpreted, and then we discuss the other elements.

6.1. Star Formation Histories from the α-elements

The α elements can be used to infer early star formation efficiency in each galaxy, as they are created primarily in the hydrostatic burning phases of massive stars and released to the interstellar medium (ISM) via Type II SNe. Because these stars are short-lived, the early enrichment in any galaxy should be dominated by enrichment from these sources. This is why nearly all dSphs have elevated [α/Fe] abundances at the lowest metallicities. At some point in [Fe/H], depending on how vigorous this initial burst of star formation was, Type Ia SNe begin to explode, enriching the ISM in heavier elements largely to the exclusion of α elements, decreasing the [α/Fe] abundance ratio while still increasing overall metallicity.

For some galaxies, the end of chemical evolution is reached shortly after Type Ia SNe begin to contribute in large quantities, as the gas is used up without replenishment. However, B. Hendricks et al. (2014) and S. Hasselquist et al. (2021) showed that later starbursts can result in flat or even increasing [α/Fe]–[Fe/H] abundance patterns. We first discuss the low-metallicity [α/Fe]–[Fe/H] values and trends and then explore which galaxies show extended SFHs and why this might be.

6.1.1. The α-element Knee

One commonly sought feature of the chemical abundance patterns of dwarf galaxies is the "knee" in the [α/Fe] abundance patterns as a function of metallicity, which represents the point at which Type Ia SNe begin to contribute to the chemical evolution of the galaxy. The metallicity at which the knee occurs is a product of the early star formation efficiency of the galaxy, with the slope of the knee being related to outflows and the overall [α/Fe] location of the knee related to the IMF. Dwarf galaxies enrich slowly, so the α-knee can occur at very low metallicities, where stochastic enrichment, mixing, and larger abundance measurement uncertainties and upper limits can lead to a large scatter in the observed abundance ratios of stars in these systems and make it difficult to identify the α-knee.

In the literature, no universal method has been adopted to measure these knees. Here we simply identify the knee as the metallicity at which the abundance trends for each galaxy cross the plateau seen in our high-α disk sample, which, except for the very most metal-poor stars, is higher than the halo +GSE sample. This self-consistent methodology avoids questions about modeling, such as species-to-species metallicity-dependent NLTE affects, and overionization. It assumes that the plateau formed by the high-α disk sample is a largely

Table 8
Chemical Evolution Knee Locations

Species	Fornax	Sculptor	Carina	Ursa Minor	Draco	Sextans	Bootes
[O/Fe]	<−2.2	−2.11:	<−2.12	−2.21:	<−2.30	<−2.32:	<−2.32
[Mg/Fe]	<−2.2	−2.07	<−2.12	−2.24:	<−2.30	<−2.32	−2.32:
[Si/Fe]	<−2.2	−2.41:	<−2.12	−2.33:	<−2.30	<−2.32	<−2.32
Adopted	<−2.2	−2.17	<−2.12	−2.26	<−2.30	<−2.32	−2.4:

pure CCSN product with a universal IMF. We report these knee metallicities in Table 8 for the three α-elements that are well measured to low metallicities in our sample, O, Mg and Si. For any galaxy that lies below the MW high-α disk sample plateau across the entire metallicity range of that galaxy as sampled here, we report the lowest-metallicity point in our sample as the upper limit on the knee position. For galaxies with measurements of knee position, we average the positions found in each element to produce our adopted α-knee measurement. For Fornax, Carina, Draco, and Sextans, we only derive upper limits for the location of the knee (between $\sim$−2.3 and −2.1) with our assumed methodology. However, for Sculptor, Ursa Minor, and Bootes I, we do measure an approximate knee location at [Fe/H] $\sim$ −2.2, −2.3, and −2.4, respectively.

These measurements have a few caveats. The first caveat is that we have assumed that the dwarf galaxies and the MW samples had a similar "plateau" at some metallicity. However, variation in the IMF can change the location of the plateau, and the element/yield/chemical evolution model choice can even make the plateau weakly sloped. A shift in the position of the plateau could change the way we would evaluate some of these chemical abundance patterns. For instance, we do see some flattening in the [α/Fe] distribution for Draco (though this corresponds to a large spread in abundances at these metallicities) that could perhaps be explained as evidence for a higher-metallicity knee combined with top-light IMF.

The second caveat is that, while we do report a measurement of the knee location for Sculptor, Ursa Minor, and Bootes I, some of these (marked with a ":" in Table 8) lie at metallicities where there are a large fraction of upper limit or nondetections in the abundance measurements. While we have chosen a method for defining the knee position that isn't dependent on finding a flattening in the [α/Fe] slope, which can be hampered by upper limits, the trends that we evaluate may still be following the stars with the highest [α/Fe] ratios at these metallicities. This makes the trends seem to rise more quickly by masking the stars that scatter to low abundance ratios. We recommend that the values we report be taken with caution; nevertheless, we can compare these knee positions with those reported in recent literature studies of these systems.

The largest sample of homogeneously analyzed dSph [α/Fe] abundance patterns was done by E. N. Kirby et al. (2011a) using medium-resolution Keck DEIMOS spectra. E. N. Kirby et al. (2011a) remarked on searching for knees in the [α/Fe] abundance patterns of eight galaxies they observe, including Fornax, Sculptor, Sextans, Draco, and Ursa Minor, which are also analyzed here. They concluded that a knee cannot be clearly detected in their data for most elements in these dwarf galaxies, though they do see a knee in the [Ca/Fe] of Sculptor at a metallicity of [Fe/H] = −1.8 and the possible detection of a knee in Ursa Minor at a slightly lower metallicity [Fe/H] $\sim$ −2. These are slightly more metal-rich than what we find here, and if the zero-point difference in [Fe/H] between the stars in common between the Kirby analysis and the APOGEE DR17 dataset is considered (−0.14 dex), then the knee would be pushed even more metal-rich in the APOGEE metallicity system. This is a fairly large discrepancy, but as pointed out in E. N. Kirby et al. (2011a), this is only seen in [Ca/Fe] and not in [Mg/Fe], [Si/Fe], or [Ti/Fe], all of which show no hint of a knee above [Fe/H] $\sim$ −2.5 (or [Fe/H] $\sim$ −2.36 in the APOGEE metallicity system), somewhat more consistent with our results. Like E. N. Kirby et al. (2011a), we do not report a clear knee for Fornax, Sextans, and Draco.

We point out that the chemical evolution models shown in Figures 2–12 of E. N. Kirby et al. (2011a) show knees below [Fe/H] $\sim$ −2.5 except Fornax, which has a model with a knee at [Fe/H] $\sim$ −1.7. A more detailed "knee" comparison with the Kirby dataset or other literature samples should be done with caution because differences in NLTE corrections from species to species, from spectral line to spectral line, and even metallicity-dependent NLTE corrections of a single spectral feature make comparisons laborious. Other effects such as differences in fitting techniques, confusion between upper limits and detections for the most metal-poor and low-S/N spectra, and abundance scale zero-points further complicate comparisons. Such a detailed analysis is beyond the scope of this work.

The low metallicities of all knees suggest that the early SFHs of these galaxies were very inefficient compared to those of the MW. However, compared to the other classical dSphs, Sculptor enriched to slightly higher metallicities before the onset of Type Ia supernova contributions. If we look at the mass of these galaxies, Sculptor is the second most-massive galaxy, behind Fornax. This suggests a correlation with stellar mass and early star formation, either because one necessarily leads to the other, or because the more-massive dark-matter halo leads to more vigorous early star formation. However, as highlighted in the left panel of Figure 11, Sculptor, perhaps unexpectedly, has a more metal-rich knee than Fornax, suggesting that Fornax must have had some sort of extended SFH, which we discuss in detail below.

6.1.2. Continuous versus Episodic Star Formation in dSph Galaxies

Although all of the dSph have metal-poor knees associated with low early star formation efficiency, the chemical evolution of these galaxies diverges at higher metallicities. Scl, UM, and Draco all have [α/Fe] abundances that continue to decline with [Fe/H] across all metallicities, suggesting that these galaxies only experienced one major epoch of star formation some time in the early Universe. This is supported in various literature photometric studies of these galaxies (e.g., M. Bettinelli et al. 2019 for Scl; e.g., R. Carrera et al. 2002; A. E. Dolphin 2002; D. R. Weisz et al. 2014b; U. Ural et al.

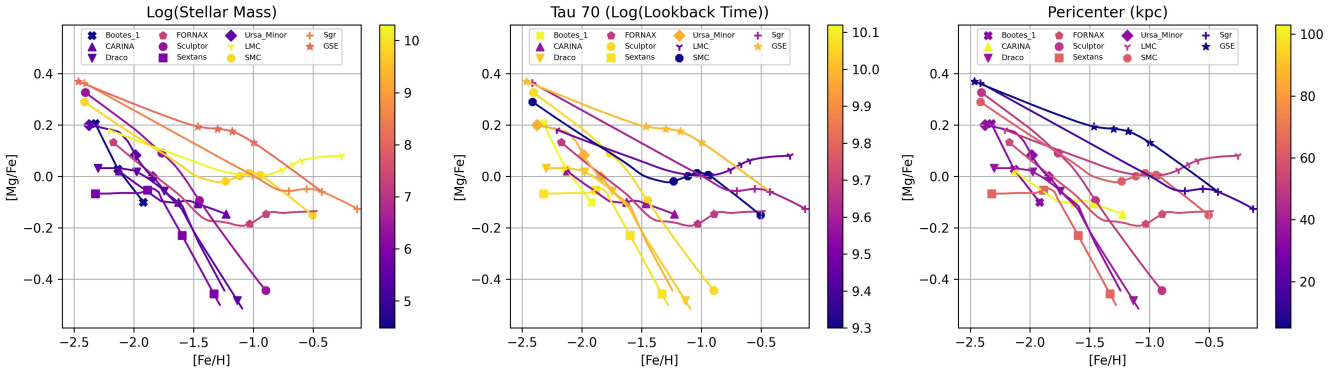

Figure 11. LOWESS curves in the [Mg/Fe]–[Fe/H] abundance plane for all galaxies studied in this work along with the APOGEE LMC, SMC, Sgr, and GSE samples studied in S. Hasselquist et al. (2021). Lines and points are colored by stellar mass in the left panel, τ_{70} in the middle panel (lookback time at which the galaxy formed 70% of its stars), and pericenter of the orbit in the right panel.

2015, for Ursa Minor and Draco), as well as chemical evolution models fit to spectroscopic data (e.g., V. Hill et al. 2019; M. A. C. de los Reyes et al. 2022). However, Carina and Fornax exhibit a flattening and even slight reversal of this trend at [Fe/H] > -1.7 for Carina and [Fe/H] > -1.1 for Fornax. This suggests that these two galaxies experienced more recent bursts of star formation, with Type II SNe contributing anew to the chemical evolution of these galaxies, raising the relative amount of Type II SNe. A second epoch of star formation that turns on relatively slowly can produce a more gradual change in chemical abundance ratios, whereas a burst can produce a jump in metallicity and abundance ratios. Al may be dependent on the available N abundance, which could be produced through slower processes such as production in AGB stars or directly by Type II SNe.

Support for later periods of star formation in Carina and Fornax can be found in the literature, both through photometric studies (e.g., A. E. Dolphin 2002; D. R. Weisz et al. 2014b, 2015) and spectroscopic studies invoking chemical evolution models (e.g., B. Hendricks et al. 2014; S. Hasselquist et al. 2021). The large spread in [Fe/H] combined with the relatively narrow red giant branch for Carina suggests that Carina experienced distinct episodic bursts compared to the more coherent chemical abundance pattern of Fornax, which S. Hasselquist et al. (2021) explained with two episodes of star formation separated by a lull.

The [α/Fe]–[Fe/H] abundance patterns that are indicative of an extended SFH have been observed in more-massive Local Group dwarf galaxies, including Sagittarius, the LMC, and the SMC (e.g., K. Bekki & T. Tsujimoto 2012; D. L. Nidever et al. 2020; S. Hasselquist et al. 2021). The left panel of Figure 11 shows the same [Mg/Fe]–[Fe/H] LOWESS lines for all galaxies studied in this work, along with the massive MW satellites from S. Hasselquist et al. (2021), colored by the mass of the galaxy. The most-massive dwarf galaxies do not show a single downward slope in their later chemical evolution. In addition, these more-massive galaxies are offset to the top-right portion of the figure, which we usually associate with a more rapid chemical evolution. The mass is clearly a very strong driver of chemical evolution; however, Carina, which shows slow but complex chemical evolution, has a lower mass than that of Sculptor and Sextans. There must be more drivers than just the galaxy mass.

The middle panel of Figure 11 displays the lookback time at which each galaxy formed 70% of its stars (τ_{70}), as inferred from the photometric SFHs of these galaxies τ_{70}. As alluded to earlier, the photometric SFHs agree with our interpretations of the [Mg/Fe]–[Fe/H] abundance patterns. Specifically, Bootes I, Sculptor, Draco, and Ursa Minor all have $\tau_{70} > 10$ Gyr. Carina and Fornax have much more recent τ_{70} values. With this color-coding, the galaxies with complex chemical evolution clearly stand out; thus, one can predict the lookback time with the shape of the [Mg/Fe]–[Fe/H] abundance trend or predict the shape of the abundance trend if the lookback time is known. However, this does not give much insight into why Carina, with its low mass, has late chemical evolution with a bursty abundance pattern.

In the right panel of Figure 11, we color the same trend lines by orbital pericenters of the galaxies. We adopt the pericenters from G. Battaglia et al. (2022; see their Table B.5) for the less-massive galaxies. For the LMC and SMC, we adopt their present-day distance from the MW as their pericenters. For Sgr, we use 15 kpc, and for GSE we use 5 kpc; although, this number is much less meaningful for GSE as it has been merged with the MW. With the exception of Sextans (and the galaxies that have already merged with the MW, e.g., GSE and Sgr), the galaxies with simple, truncated SFHs are much closer to the MW (i.e., have much smaller orbital pericenters) than those with extended SFH. Carina happens to be the galaxy with the farthest pericenter. So, while mass likely plays a role in determining the early SF efficiency of a galaxy, the galactic environment, specifically proximity to the MW, in this case, plays a role in determining the extent to which a galaxy exhibits future episodes of SF. These episodes likely come in the form of galaxy–galaxy interactions, but interactions that have much more similar mass ratios, i.e., not with MW-sized galaxies. GSE and Sgr stand out as peculiar in this trend of pericenter and late stage burstyness. In this case, the pericenter may be misleading; for example, Ruiz-Lara et al. (2020) reported that Sgr may have had its first infall with the MW 5 Gyr ago, giving Sgr a long period to evolve and undergo small mergers creating bursts before a single first orbital encounter. The chemical evolution of a galaxy is driven both by its inherent properties, such as mass, but also by its environmental properties, such as proximity to massive galaxies (stripping and quenching) and smaller galaxies (bursts and infall).

Sextans appears to be somewhat of an exception to this rule. It has a relatively low mass, but more massive than its apparent knee might suggest. Moreover, it has much less recent τ_{70} values than we might infer from its larger pericenter distance. However, unlike the dSphs that show simple SFH, Sextans apparently never reaches solar [Mg/Fe] at the lowest metallicities studied by APOGEE. If we consider the literature and the APOGEE observations of Sextans (panel (f) of Figure 10) together, we infer that Sextans actually may have a very

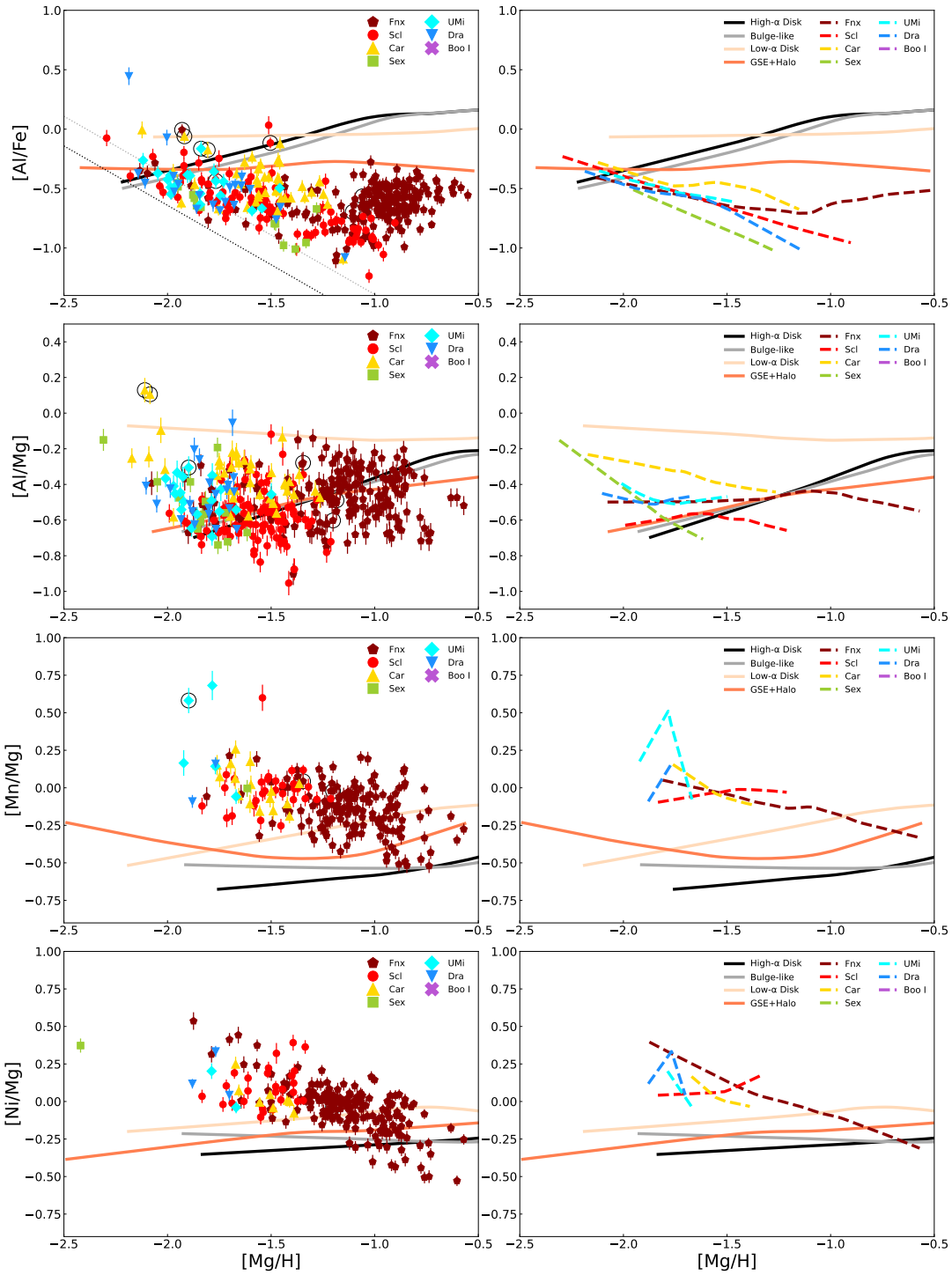

Figure 12. Similar to Figure 7 but using [Mg/H] as the metallicity source.

complicated [Mg/Fe]–[Fe/H] abundance pattern, one that is similar to that of Carina but shifted to much lower metallicity. Sextans has less literature indicating multiple episodes of star formation, with studies finding that Sextans formed most of its stars early in its SFH, although a small number of stars may have been formed up to 7 Gyr ago (M. G. Lee et al. 2009; M. Bettinelli et al. 2018). However, other studies have found evidence for kinematically distinct components of Sextans that could indicate that it has had previous mergers that could have driven a burst of star formation or prolonged star formation in Sextans (J. T. Kleyna et al. 2004; G. Battaglia et al. 2011; S. Okamoto et al. 2017; L. Cicuéndez & G. Battaglia 2018). Future spectroscopic surveys that target Sextans stars across the full metallicity range will shed light on whether Sextans is an apparent exception to the mass-environment rule discussed above.

6.2. Metallicity-dependent Yields

Most of the elements for which we have been able to derive abundances have origins in CCSNe and/or Type Ia SNe (and to a lesser extent, AGB stars). If we use Mg as a proxy for pure

CCSNe, then the elements with declining [X/Mg] abundance ratios with increasing metallicity either have contributions from Type Ia SN or have metallicity-dependent CCSN yields; see Figure 12. Additionally, elements with trends of [X/Mg] that are different from those of the CCSN-dominated MW samples (bulge/halo/high-alpha disk) have significant Type Ia SN contributions or have metallicity-dependent CCSN yields.

However, for Carina and Fornax, which show evidence of a burst in their star formation, we have some leverage to understand the relative contributions. The elements that show discontinuity at the burst Fe metallicity in Carina are O, Mg, Si, and possibly Al, Mn, and C. The first three are well understood to be alpha elements. For the last three, the number of true detections below the burst is very small to be definitive, but the median value at the burst is higher than that of the other dSph, suggesting that there may be an extra contribution above the scaled solar amount produced in CCSN. It is the pre-burst stars in Carina that exhibit anomalous [Al/Mg] ratios; the more metal-rich burst stars exhibit [Al/Mg] ratios more consistent with the other dwarf galaxies and the CCSN-dominated MW samples. We also note that Sextans exhibits a rising Al abundance trend as a function of declining metallicity, similar to Carina and to a lesser extent the low-alpha disk.

The elements that show discontinuity at the burst Fe metallicity in Fornax are C, N, O, Mg, Si, Ca, Al, and Mn. In addition to O and Mg, the elements that show the strongest rise include C, and Al, which may have contributions from many possible sources, e.g., whatever mechanism enriches second-generation globular cluster stars. The relatively smaller increases in Ca and Mn in the burst populations hint at metallicity-dependent yields.

7. Summary

1. We performed a detailed membership analysis of the 1315 targets in the vicinity of seven dSphs using Gaia EDR3 proper motions and APOGEE DR17 radial velocities. We consider 731 targets as members of their respective dSph. Of these, 528 or 72% have reliable ASPCAP stellar parameters.
2. We developed a method to distinguish between true measurements and upper limits in ASPCAP results using synthetic spectra of metal-poor giants ([Fe/H] $= -1$, $\log g = 1.0$) over the following ranges: $T_{\rm eff} = 4200$–4800 K and [X/H] $= -2.5$ to -0.5. This was completed for 17 elements. The number of stars in each dSph with reliable chemical abundance detections is given in Table 5. We provide these data to the community. High-quality abundances with few upper limits are determined for oxygen, magnesium, aluminum, silicon, and iron. For elements carbon, nitrogen, calcium, manganese, and nickel, we determined that we are dominated by upper limits for the more metal-poor and lower-S/N spectra; thus, the trends at the metal-poor end for these elements are not constrained. We note that for sodium and vanadium, we find no detections in our sample, and for potassium, sulfur (marginally), chromium, cobalt, and cerium, there are only detections for the most metal-rich and highest-S/N observations. We warn the community to be extremely careful in using DR17 abundances for these elements with low-S/N spectra of low-metallicity or warm stars.
3. Figure 2 has the color–magnitude diagram for the final dSph sample. The APOGEE DR17 sampling spans ∼1.0 to ∼1.5 mag on the upper giant branch for all but Fornax. In addition to the RGB, we have stars selected from the AGB and above the RGB.
4. We produced visualizations of the abundance distributions for 16 independent abundance planes (including [(C+N)/Fe] and [C/N]) and compared them to comparison samples in four Milky Way structures. Where more than 50% of the sample has measured abundances (versus upper limits), we produce median trend lines.
5. We combined APOGEE observations with high-resolution studies in the literature, many of which extend to significantly lower [Fe/H]. We demonstrate how chemical abundance patterns provide insight into the SFH and constrain the level of SFR in course values. We separated into continuous and episodic SFH based on the chemical abundance patterns.

Acknowledgments

This material is based on work supported by the National Science Foundation under grant No. 2206514. S.H. acknowledges support from the STScI DDRF.

Funding for the Sloan Digital Sky Survey IV has been provided by the Alfred P. Sloan Foundation, the U.S. Department of Energy Office of Science, and the Participating Institutions. SDSS-IV acknowledges support and resources from the Center for High-Performance Computing at the University of Utah. The SDSS website is www.sdss.org.

SDSS-IV is managed by the Astrophysical Research Consortium for the Participating Institutions of the SDSS Collaboration including the Brazilian Participation Group, the Carnegie Institution for Science, Carnegie Mellon University, the Chilean Participation Group, the French Participation Group, Harvard-Smithsonian Center for Astrophysics, Instituto de Astrofísica de Canarias, The Johns Hopkins University, Kavli Institute for the Physics and Mathematics of the Universe (IPMU) / University of Tokyo, Lawrence Berkeley National Laboratory, Leibniz Institut für Astrophysik Potsdam (AIP), Max-Planck-Institut für Astronomie (MPIA Heidelberg), Max-Planck-Institut für Astrophysik (MPA Garching), Max-Planck-Institut für Extraterrestrische Physik (MPE), National Astronomical Observatory of China, New Mexico State University, New York University, University of Notre Dame, Observatário Nacional / MCTI, The Ohio State University, Pennsylvania State University, Shanghai Astronomical Observatory, United Kingdom Participation Group, Universidad Nacional Autónoma de México, University of Arizona, University of Colorado Boulder, University of Oxford, University of Portsmouth, University of Utah, University of Virginia, University of Washington, University of Wisconsin, Vanderbilt University, and Yale University.

This publication makes use of data products from the Two Micron All Sky Survey, which is a joint project of the University of Massachusetts and the Infrared Processing and Analysis Center/California Institute of Technology, funded by the National Aeronautics and Space Administration and the National Science Foundation.

This work is based, in part, on observations made with the Spitzer Space Telescope, which is operated by the Jet Propulsion Laboratory, California Institute of Technology under a contract with NASA.

This publication makes use of data products from the Wide-field Infrared Survey Explorer (WISE; E. L. Wright et al. 2010), which is a joint project of the University of California, Los Angeles, and the Jet Propulsion Laboratory/California Institute of Technology, funded by the National Aeronautics and Space Administration, and NEOWISE, which is a project of the Jet Propulsion Laboratory/California Institute of Technology. WISE and NEOWISE are funded by the National Aeronautics and Space Administration

This work has made use of data from the European Space Agency (ESA) mission Gaia (https://www.cosmos.esa.int/gaia), processed by the Gaia Data Processing and Analysis Consortium (DPAC, https://www.cosmos.esa.int/web/gaia/dpac/consortium). Funding for the DPAC has been provided by national institutions, in particular the institutions participating in the Gaia Multilateral Agreement.

This research has made use of NASA's Astrophysics Data System.

This research has made use of the SIMBAD database, operated at CDS, Strasbourg, France. The original description of the SIMBAD service was published in M. Wenger et al. (2000).

This research has made use of the VizieR catalog access tool, CDS, Strasbourg, France (DOI: 10.26093/cds/vizier). The original description of the VizieR service was published F. Ochsenbein et al. (2000).

Facilities: Du Pont (APOGEE), Sloan (APOGEE), Spitzer, WISE, CTIO:2MASS, FLWO:2MASS, Gaia.

Software: Astropy (Astropy Collaboration et al. 2013, 2018), Doppler (D. Nidever 2021), NumPy (S. van der Walt et al. 2011; C. R. Harris et al. 2020), TopCat (M. B. Taylor 2005), Turbospectrum (B. Plez 2012; R. Alvarez & B. Plez 1998).

Appendix A
Additional dSph Membership Discussion

A.1. Nonmembers Targeted as Members

There are 46 targets that were targeted based on literature data but are not classified as members in this work (or in DR17). Some of these do not have ASPCAP results because the total S/N of the spectrum is <5. Although the final S/N is between 5 and 32, another subset of targets have very poor spectral quality typified with no identifiable features, poor RV templates, and, most likely, spurious ASPCAP results. Some of these, however, do have radial velocities consistent with the targeted dSph, but other aspects of the RV measurements are concerning (for example, the visit-level cross-correlation peaks are marginal). These low-S/N objects are indicated in Figure 1 as targeted members (orange) not classified as members in APOGEE/this work (open) and with a black "*x*" to indicate the poor data quality.

As given in Table 9, there are 13 targets with reliable spectra (based on visual inspection) that we reclassify as nonmembers and one target that is a one of the Fornax GCs that had poor Gaia EDR3 results. Seven of these have dwarf-like stellar parameters from the APOGEE spectra, but all 13 fail the astrometric criteria. Because the astrometry is subject to change with future Gaia releases, the five stars that are spectroscopic giants may be reclassified in the future.

A.2. Detailed Star-by-star Assessments

There are 23 additional stars among the seven dSphs that are classified as members in this work but not in the MEMBER convenience flag. The members not indicated in DR17 via the MEMBER tag are listed in Table 10.

There are 12 stars that were excluded from this analysis because their ASPCAP solutions were unrealistic, e.g., dwarf surface gravity, unrealistically hot or cool. We list these stars in Table 11. In many cases, the S/N is low, so a poor APOGEE solution is not surprising; however, for a few with very good S/Ns, they are luminous AGB stars and likely variables, which means that the combination of many epochs of spectra probably results in a nonsense solution.

Table 9
APOGEE Nonmembers Classified as Members in the Literature

APOGEE_ID	dSph	Lit. Membership	SNREV	Notes
2M06405987-5100423	Carina	2MASS Blend, fiber target nonmember	178	dwarf stellar parameters; Astrometric nonmember
2M06410358-5057048	Carina	M. G. Walker et al. (2009)	56	Astrometric nonmember
2M06420906-5058365	Carina	M. G. Walker et al. (2009)	37	dwarf stellar parameters; Astrometric nonmember
2M06391906-5106303	Carina	2MASS Blend, fiber target nonmember	34	dwarf stellar parameters; Astrometric nonmember;
2M17210799+5720370	Draco	M. G. Walker et al. (2015)	93	Astrometric nonmember;
2M17212624+5752066	Draco	T. E. Armandroff et al. (1995)	71	dwarf stellar parameters; Astrometric nonmember
2M02400793-3437162	Fornax	M. G. Walker et al. (2009)	59	Astrometric nonmember;
2M02401001-3429589	Fornax	M. Mateo et al. (1991)	49	Astrometric nonmember;
2M02395022-3435595	Fornax	M. G. Walker et al. (2009)	55	Astrometric nonmember;
2M10130818-0144502	Sextans	M. G. Walker et al. (2009)	37	dwarf FERRE results; Astrometric nonmember
2M15125534+6748381	Ursa Minor	C. Palma et al. (2003) (photometry only)	62	Astrometric nonmember; Binary?
2M02394817-3415285	Fornax	⋯	217	GC Fornax H3; Poor Gaia EDR3 results
2M01014472-3338305	Sculptor	Targeting Flag Error	59	dwarf stellar parameters; Astrometric nonmember
2M00590484-3342548	Sculptor	Targeting Flag Error	57	dwarf stellar parameters; Astrometric nonmember

Table 10
Additional dSph Members in the 6σ Sample

APOGEE_ID	dSph
2M14001049+1431454	Bootes I
2M14011845+1415250	Bootes I
2M14035451+1453285	Bootes I
2M06394720–5057439	Carina
2M06415434–5102460	Carina
2M17184293+5738497	Draco
2M17193185+5733347	Draco
2M02394528–3431581	Fornax
2M02400555–3428374	Fornax
2M02400770–3432103	Fornax
2M02410076–3419005	Fornax
2M02410892–3434232	Fornax
2M02415773–3437015	Fornax
2M01000007–3338343	Sculptor
2M01004017–3334353	Sculptor
2M10121623–0144455	Sextans
2M10122620–0138301	Sextans
2M10122701–0130214	Sextans
AP10123769–0211303	Sextans
2M10123857–0129189	Sextans
2M10134122–0206086	Sextans
2M10152592–0204318	Sextans
2M15063038+6656411	Ursa Minor

Table 11
Stars Excluded Based on Parameter Range

APOGEE_ID	Galaxy	SNREV	Notes
2M17203116+5758060	Draco	22	Note 1
2M15030656+6723166	Ursa_Minor	41	Note 1
2M10115110–0154426	Sextans	44	Note 1
AP10123769–0211303	Sextans	16	Note 1
2M10130429–0134589	Sextans	19	Note 1
2M10152592–0204318	Sextans	135	Note 1, Carbon Star
2M10153545–0131108	Sextans	20	Note 1
2M00590406–3340317	Sculptor	26	Note 1
2M00593045–3336050	Sculptor	29	Note 1
2M01012084–3353047	Sculptor	127	Note 1, Mira
2M01021830–3337358	Sculptor	16	Note 1
2M01024977–3340378	Sculptor	14	Note 1
2M06404244–5100428	CARINA	33	Note 1
2M02384457–3448255	FORNAX	90	Note 1

Note. [1]ASPCAP stellar parameters out of reasonable range

A.3. Carbon Stars in High-quality Sample

A.3.1. Literature Classifications, but No Carbon Enhancement

The following stars in our main sample are listed as C* in SIMBAD, but the ASPCAP solution shows little carbon enhancement. CARINA:2M06403082-5059153, CARINA:2M06404775-5106033, CARINA:2M06411470-5051099, CARINA:2M06414823-5055016, FORNAX:2M02395861-3425279.

A.4. ASPCAP-identified Carbon Stars

We identified carbon stars on the basis of their carbon abundance, stellar parameters, and spectral identification. The details of these identifications will be presented in a companion paper, but for completeness in our data file and sample, we include the identifications here. More specifically, candidate carbon stars are flagged. We further note stars previously identified as carbon stars that have no clear carbon enhancement in our spectra.

Appendix B
Derivation of Upper-limit Formula

Our upper-limit methodology is driven by the following idea: for a given abundance measurement to be considered a detection, the average line depth of the relevant lines of that element should exceed the noise on that average. So by measuring the average line depth of the lines that APOGEE uses to measure abundances of each element, and by setting some threshold χ, such that the average line depth is χ times larger than the spectral noise averaged over those lines, we can provide an estimate of what S/N we need to measure that abundance.

Since it begins to become cost prohibitive to estimate this S/N for every abundance measurement, we instead estimate these S/N thresholds at a range of relevant abundances and temperatures and use this to produce the upper-limit relations we report in this paper. Our procedure to do this is as follows.

1. Produce synthetic spectra with the element of interest, and spectra where the lines of that element are missing.
2. From the difference spectra, measure the weighted-average line depth, using APOGEE's window weights for that element.
3. Calculate the S/N threshold needed to measure the abundance of that element.
4. Repeat this process at a range of temperatures and abundances.
5. Fit a polynomial model for the abundance upper limit as a function of temperature and S/N for each element.
6. Use these polynomial models to flag APOGEE measurements that are likely upper limits according to our choice of threshold.

B.1. Synthetic Spectra Grids

For the non-CNO elements that we analyze, we calculate synthetic spectra at a range of temperatures from $T_{\rm eff} = 4200$–4800 K in steps of 200 K, and at a range of abundances from [X/H] $= -2.5$ to -0.5 in steps of 0.5 dex, with [Fe/H] $= -1.0$, $\log g = 1.0$, $v_{\rm micro} = 2$, and hold all other abundances solar-scaled. And then repeat these calculations decreasing the [X/Fe] abundance by -5 to simulate removing the lines of that element.

Most elements are measured from atomic lines; however, C, N, and O are primarily measured from molecular lines (in particular CO, CN, and OH), whose line strengths are interdependent on the abundances of each element, so we use two slightly different temperature and abundance grids to calculate their abundances.

For C, N, and O, we again calculate synthetic spectra at a range of temperatures from $T_{\rm eff} = 4200$–4800 K in steps of 200 K, but then at a range of metallicities from [Fe/H] $= -2.5$ to -0.5 in steps of 0.5 dex. We do this while holding [C/Fe] $= -0.75$, [N/Fe] $= 0.25$ and O at solar-scaled, which are typical values seen in our dSph sample. And again we use $\log g = 1.0$, $v_{\rm micro} = 2$, and hold all other abundances solar-scaled. To simulate the lack of C, N, and O features, instead of

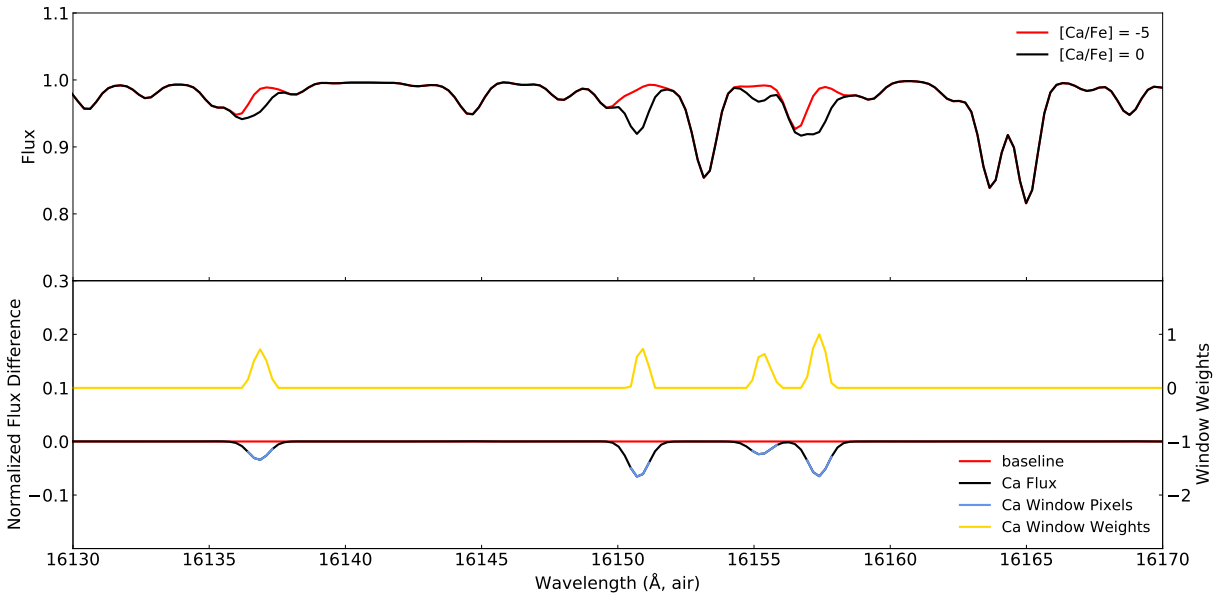

Figure 13. Top panel: normalized synthetic spectra at a temperature of 4200 K, metallicity of [Fe/H] −1, and [Ca/Fe] = 0 (black) and −5 (red). Bottom panel: difference of the solar Ca abundance spectrum and no Ca spectrum (black), the null difference (red), along with the APOGEE window strengths (yellow). Pixels in the difference spectra where the window strengths are nonzero are highlighted (blue).

reducing the abundances of any of these elements, which are important to the molecular equilibrium in stellar atmospheres, we instead repeat these syntheses but with line lists that have the relevant lines removed for each element (CO, CN, and C I lines removed for C, CN removed for N, and CO and OH removed for O).

Using the above parameters and abundances, we synthesize spectra using the 1D LTE Turbospectrum (v19.1.4) radiative transfer code (B. Plez 2012; R. Alvarez & B. Plez 1998), with spherical radiative transfer and using the MARCS model atmosphere grid (B. Gustafsson et al. 2008). For consistency with ASPCAP's abundance determinations, we use the APOGEE DR17 Turbospectrum line list, version *180901t20*. We synthesize the relevant wavelength range for each element in steps of 0.05 Å and then convolve these spectra with a Gaussian profile with an FWHM of 800 mÅ to account for typical instrumental resolution, and then convolve them with a Gaussian velocity profile of 5 km s^{-1}, to account for typical macroturbulent velocity broadening. Finally we interpolate the synthetic spectra and resample them to APOGEE's wavelength scale.

B.2. Measuring S/N Thresholds

From our calculations, we have pairs of synthetic spectra with and without the element, X, in question. We used these spectra, combined with APOGEE's window weights for that element to measure the S/N threshold needed to detect this abundance-temperature combination. In the following, we provide a case study of this procedure with Ca as our example element.

In the top panel of Figure 13, we show our pair of synthetic spectra at $T_{\rm eff}$ = 4200 K and [Fe/H] = −1 with [Ca/Fe] = 0 and [Ca/Fe] = −5, around the region that APOGEE uses to measure Ca. We then take the difference between these two synthetic spectra, which is shown in the bottom panel of Figure 13. The difference spectrum indicates the flux from the Ca lines at an abundance of [Ca/H] = −1. We then measure a weighted-average Ca line depth by taking a weighted average of the difference spectrum, weighted by the APOGEE Ca window weights for each pixel, which are shown as the gold line in Figure 13. Numerically this is:

$$D_{\rm wavg} = \frac{\sum_i w_i D_i}{\sum_i w_i},$$

where w_i is the window weight, and D_i is the Ca flux from the difference spectrum, for pixels i. For this example, the weighted-average line depth is 0.0416, across a weighted number of pixels, $N_{\rm wavg} = \sum_i w_i$ = 8.35. We then use this weighted-average line depth to estimate the S/N threshold needed to confidently detect Ca in the [Ca/Fe] = 0 spectrum. For a given S/N, the noise per pixel in a normalized spectrum would be $\sigma_{\rm pix} = 1/({\rm S/N})$. When averaging this noise over the $N_{\rm wavg}$, the error we would expect on measuring $D_{\rm wavg}$ would be

$$\sigma_{\rm wavg} = \frac{\sigma_{\rm pix}}{\sqrt{N_{\rm wavg}}} = \frac{1}{{\rm S/N} \cdot \sqrt{N_{\rm wavg}}}.$$

We therefore have an estimate of our Ca "signal," $D_{\rm wavg}$, and the expected error on this measurement for a given S/N, $\sigma_{\rm wavg}$; all that remains is to set a threshold, χ, above which the measurement would be considered a confident detection. Traditionally, studies will consider a (χ =) 3σ–5σ signal for detection depending on the circumstances. Since our procedure has made a number of assumptions and is likely a fairly simple estimate, we have chosen to use $\chi = 4$ as our threshold, which we have verified is reasonable by comparing with previous literature measurements and through a visual inspection of cases near these thresholds. Stating this another way, we use a detection threshold of 4σ.

This choice allows us to work backward and determine the equivalent S/N threshold needed to measure a given $D_{\rm wavg}$ that we are able to measure from synthetic spectra. Specifically, this S/N threshold can by found with some

rearrangement:

$$S/N_{limit} = \frac{4}{D_{wavg}\sqrt{N_{wavg}}}.$$

For our example of [Ca/H] = −1, with D_{wavg} measured over N_{wavg} = 8.35 pixels, the S/N threshold for a measurement would be S/N_{limit} = 33.3.

B.3. Deriving Upper-limit Relations

In order to turn individual S/N limit measurements into more general upper-limit relations, we first measure S/N thresholds for each element, temperature, and abundance combination. We then fit these with a polynomial surface to provide a parameterized upper-limit threshold using the following functional form:

$$[X/H]_{limit} = \alpha + \beta\left(\frac{T_{eff}}{1000\ K}\right) + \gamma \log_{10}(S/N) + \delta[(\log_{10}(S/N))]^2 . \quad (B1)$$

The residuals between the calculated thresholds and the polynomial fits are below 0.1 dex and, therefore, should provide a reasonable estimate of the detection threshold. Although, we note that these estimates are designed to remove the most egregious cases of nondetections and may be less discriminatory for marginal detections.

An example of one of these limit thresholds is shown for Ca in Figure 14. We have quantized the color map for simplicity of visual interpretation, but note that the actual thresholds as implemented are continuous functions of S/N and temperature. This shows a typical case, where the upper limits are higher for lower-S/N stars and warmer stars.

B.3.1. Notes on Individual Elements

Sodium (Na). On the basis of our upper-limit analysis for Na, we determined that Na is not detectable in the dSph sample except for one cool, metal-rich Fornax star. The upper limits we compute are typically >0.2 dex and, thus, do not constrain chemical evolution in these dSphs.

Sulfur (S). Although the formula we derive for upper limits does reject 93% of the sample, the remaining 7% are extremely supersolar (mean [S/Fe] > + 0.73). As mentioned above, the nature of our methodology can result in a detection being generated from very high [S/Fe] scattered false positives. Inspection of the spectra does not reveal any believable detections. The upper limits are typically >0.3 dex, so they do not provide interesting constraints on dSph nucleosynthesis.

Vanadium (V). Based on our upper-limit analysis for V, we determine that V is not detectable in the dSph sample except for six cool, metal-rich Fornax stars, and two of these have unrealistically high detections and are likely false positives. The remaining four points have a mean [V/Fe] of −0.46 at a mean [Fe/H] = −0.75. The upper limits we compute are typically >1.0 dex and, thus, do not constrain chemical evolution in these dSph.

B.3.2. Notes on Metallicity

Iron (Fe). As a primary metallicity indicator, [Fe/H] is critical for the analysis and interpretation of the dSph abundance patterns. Based on our analysis, there are 25 stars that should be removed from the dSph sample because

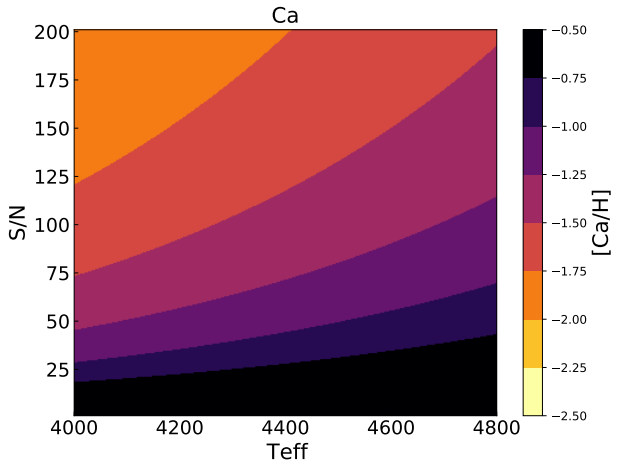

Figure 14. Derived upper limits for Ca as a function of temperature and S/N.

[Fe/H] should not be detectable. In the V. Hill et al. (2019) and E. N. Kirby et al. (2010) cross-matched samples, only one star is removed from each sample based on the upper limits of [Fe/H]. The agreement with Hill is excellent, while there is a large miss-match with Kirby. This suggests that some stars that have been removed from our sample based on our upper limits could be marginally detectable. We will exclude the 25 Fe upper-limit stars from discussions and figures that involved [Fe/H].

Magnesium (Mg). [Mg/H] is an alternative metallicity indicator that will be used in this analysis. Based on our formula, there are 12 stars with undetectable Mg lines. Visual inspection of these 12 stars' spectra reveals that the strongest lines within the APOGEE windows remain detectable in some of the stars, while they are not detectable in others. We take a consistent and conservative approach and remove the 12 Mg upper-limit stars from discussions and figures that use [Mg/H] as a metallicity indicator.

Appendix C
Comparison Samples

When showing the dSph abundance patterns in Figures 5–8 of Section 4, we include a MW comparison sample also observed by APOGEE to help put the dSph abundance patterns in a greater galactic context. Starting from the full DR17 APOGEE catalog, we perform the following restrictions:

1. remove stars associated with the LMC and SMC using the spatial and kinematic cuts given in S. Hasselquist et al. (2021);
2. remove the Sgr dSph and stream stars that are presented in C. R. Hayes et al. (2020) and S. Hasselquist et al. (2021);
3. remove any stars labeled as a cluster or dSph member using the `MEMBER` flag in the allStar file;
4. remove stars with `STAR_BAD`, `M_H_BAD`, or `ALPHA_M_BAD`;
5. remove any duplicate observations;
6. and finally, we use only the stars that should provide the highest-quality abundance measurements, namely those with `SNREV` > 100, $\log g$ < 4.0, T_{eff} < 5500 K, metallicities, [Fe/H] < −0.5.

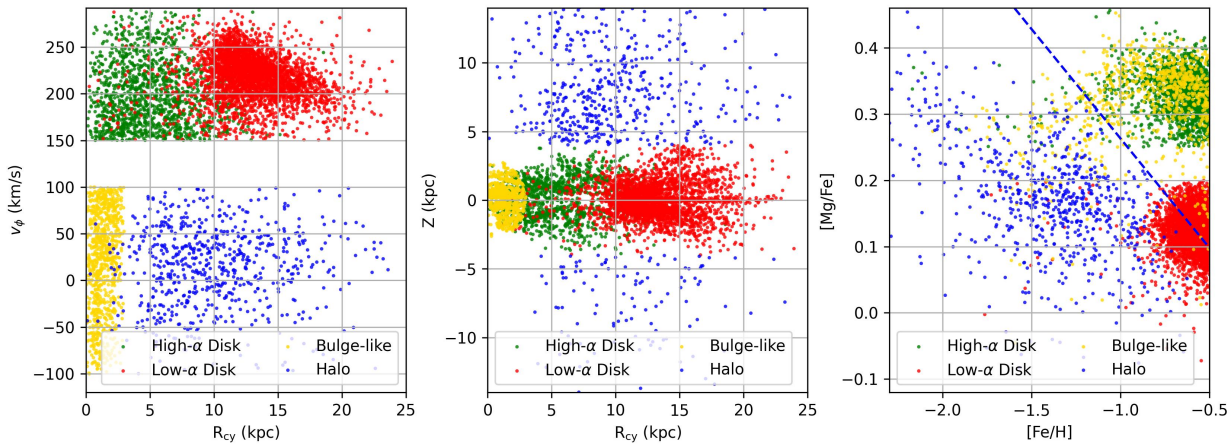

Figure 15. Visualizations of the MW Comparison sample used in various figures throughout the main text. The left panel shows Galactic rotational velocity, v_ϕ, as a function of Galactic cylindrical radius ($R_{GC,\,cy}$), and the middle panel shows distance from Galactic plane, Z, plotted as a function of $R_{GC,\,cy}$. The right panel shows the [Mg/Fe]–[Fe/H] abundance plane. All parameters shown here are used to divide the MW comparison sample into the subsamples listed in the legend, as described in the text.

Once these cuts were performed, the remaining stars had their positions and velocities transformed into a Galactocentric frame. To do so, we used `StarHorse` spectro-photometric distances (B. X. Santiago et al. 2016; A. B. A. Queiroz et al. 2018, 2020; F. Anders et al. 2019) assuming $R_{GC,\odot} = 8.122$ kpc (Gravity Collaboration et al. 2018). We additionally used the D. R. H. Johnson & D. R. Soderblom (1987) method to transform the APOGEE radial velocities and Gaia EDR3 proper motions to heliocentric 3D spatial velocities, and convert these to Galactocentric space velocities assuming a total solar motion of $(V_r,\ V_\phi\ V_z)_\odot = (14, 253, 7)\,\mathrm{km\,s^{-1}}$ in the right-handed velocity sense (R. Schönrich et al. 2010; R. Schönrich 2012; C. R. Hayes et al. 2018).

With these Galactocentric positions and velocities, we define four MW comparison samples as follows:

1. High-α disk sample: $150 < v_\phi < 290$ km s^{-1}, [Mg/Fe] > 0.25, $|z| < 4$ kpc, and $\log g < 1.3$ (to limit the sample to a similar range as the dSph stars);
2. Low-α disk sample: $150 < v_\phi < 290$ km s^{-1}, [Mg/Fe] < 0.2, $|z| < 4$ kpc, and $\log g < 1.3$;
3. Bulge-like sample: $-100 < v_\phi < 100$ km s^{-1}, $|R_{GC,\,sph}| < 3$ kpc, and $\log g < 1.3$;
4. Halo sample: $-100 < v_\phi < 100$ km s^{-1}, [Mg/Fe] $< -0.333 \cdot$ [Fe/H] -0.067, $|z| > 4$ kpc, and $\log g < 1.3$.

These MW comparison samples are shown in Figure 15, where we plot the parameters used to separate these samples. We find that the halo sample primarily comprises GSE stars, so we refer to this sample as "GSE+Halo" in the text for clarity.

ORCID iDs

Matthew Shetrone https://orcid.org/0000-0003-0509-2656
Rachael L. Beaton https://orcid.org/0000-0002-1691-8217
Christian R. Hayes https://orcid.org/0000-0003-2969-2445
Sten Hasselquist https://orcid.org/0000-0001-5388-0994
Joshua D. Simon https://orcid.org/0000-0002-4733-4994
Jon A. Holtzman https://orcid.org/0000-0002-9771-9622
Katia Cunha https://orcid.org/0000-0001-6476-0576
Steven R. Majewski https://orcid.org/0000-0003-2025-3147
Jennifer Sobeck https://orcid.org/0000-0002-4989-0353
Ricardo Schiavon https://orcid.org/0000-0002-2244-0897
Thomas Masseron https://orcid.org/0000-0002-6939-0831
Verne V. Smith https://orcid.org/0000-0002-0134-2024
David L. Nidever https://orcid.org/0000-0002-1793-3689

References

Abdurro'uf, Accetta, K., Aerts, C., et al. 2022, ApJS, 259, 35
Allende Prieto, C., Beers, T. C., Wilhelm, R., et al. 2006, AJ, 636, 804
Alvarez, R., & Plez, B. 1998, A&A, 330, 1109
Anders, F., Khalatyan, A., Chiappini, C., et al. 2019, A&A, 628, A94
Aoki, W., Arimoto, N., Sadakane, K., et al. 2009, A&A, 502, 569
Armandroff, T. E., Olszewski, E. W., & Pryor, C. 1995, AJ, 110, 2131
Astropy Collaboration, Price-Whelan, A. M., Sipőcz, B. M., et al. 2018, AJ, 156, 123
Astropy Collaboration, Robitaille, T. P., Tollerud, E. J., et al. 2013, A&A, 558, A33
Battaglia, G., Taibi, S., Thomas, G. F., & Fritz, T. K. 2022, A&A, 657, A54
Battaglia, G., Tolstoy, E., Helmi, A., et al. 2011, MNRAS, 411, 1013
Beaton, R. L., Oelkers, R. J., Hayes, C. R., et al. 2021, AJ, 162, 302
Bekki, K., & Tsujimoto, T. 2012, ApJ, 761, 180
Bergemann, M., Collet, R., Amarsi, A. M., et al. 2017, ApJ, 847, 15
Bettinelli, M., Hidalgo, S. L., Cassisi, S., Aparicio, A., & Piotto, G. 2018, MNRAS, 476, 71
Bettinelli, M., Hidalgo, S. L., Cassisi, S., et al. 2019, MNRAS, 487, 5862
Blanton, M. R., Bershady, M. A., Abolfathi, B., et al. 2017, AJ, 154, 28
Bonanos, A. Z., Stanek, K. Z., Szentgyorgyi, A. H., Sasselov, D. D., & Bakos, G. Á. 2004, AJ, 127, 861
Bowen, I. S., & Vaughan, A. H. 1973, ApOpt, 12, 1430
Carrera, R., Aparicio, A., Martínez-Delgado, D., & Alonso-García, J. 2002, AJ, 123, 3199
Casey, A. R., Hogg, D. W., Ness, M., et al. 2016, arXiv:1603.03040
Cicuéndez, L., & Battaglia, G. 2018, MNRAS, 480, 251
Cohen, J. G., & Huang, W. 2009, ApJ, 701, 1053
Cohen, J. G., & Huang, W. 2010, ApJ, 719, 931
Dall'Ora, M., Clementini, G., Kinemuchi, K., et al. 2006, ApJL, 653, L109
de los Reyes, M. A. C., Kirby, E. N., Ji, A. P., & Nuñez, E. H. 2022, ApJ, 925, 66
Dolphin, A. E. 2002, MNRAS, 332, 91
Feltzing, S., Eriksson, K., Kleyna, J., & Wilkinson, M. I. 2009, A&A, 508, L1
Frebel, A., Norris, J. E., Gilmore, G., & Wyse, R. F. G. 2016, ApJ, 826, 110
Gaia Collaboration, Brown, A. G. A., Vallenari, A., et al. 2018, A&A, 616, A1
García Pérez, A. E., Allende Prieto, C., Holtzman, J. A., et al. 2016, AJ, 151, 144
Geisler, D., Villanova, S., O'Connell, J. E., et al. 2021, A&A, 652, A157
Gilmore, G., Norris, J. E., Monaco, L., et al. 2013, ApJ, 763, 61
Gratton, R. G., Sneden, C., Carretta, E., & Bragaglia, A. 2000, A&A, 354, 169
Gravity Collaboration, Abuter, R., Amorim, A., et al. 2018, A&A, 618, L10
Gunn, J. E., Siegmund, W. A., Mannery, E. J., et al. 2006, AJ, 131, 2332

Gustafsson, B., Edvardsson, B., Eriksson, K., et al. 2008, A&A, 486, 951
Harris, C. R., Millman, K. J., van der Walt, S. J., et al. 2020, Natur, 585, 357
Hasselquist, S., Shetrone, M., Smith, V., et al. 2017, ApJ, 845, 162
Hasselquist, S., Hayes, C. R., Lian, J., et al. 2021, ApJ, 923, 172
Hayes, C. R., Law, D. R., & Majewski, S. R. 2018, ApJL, 867, L20
Hayes, C. R., Majewski, S. R., Hasselquist, S., et al. 2020, ApJ, 889, 63
Hayes, C. R., Masseron, T., Sobeck, J., et al. 2022, ApJS, 262, 34
Hendricks, B., Koch, A., Walker, M., et al. 2014, A&A, 572, A82
Hill, V., Skúladóttir, Á., Tolstoy, E., et al. 2019, A&A, 626, A15
Hubeny, I., & Lanz, T., 2011 Synspec: General Spectrum Synthesis Program, Astrophysics Source Code Library, ascl:1109.022
Irwin, M., & Hatzidimitriou, D. 1995, MNRAS, 277, 1354
Ishigaki, M. N., Aoki, W., Arimoto, N., & Okamoto, S. 2014, A&A, 562, A146
Jablonka, P., North, P., Mashonkina, L., et al. 2015, A&A, 583, A67
Jenkins, S. A., Li, T. S., Pace, A. B., et al. 2021, ApJ, 920, 92
Ji, A. P., Simon, J. D., Roederer, I. U., et al. 2023, AJ, 165, 100
Johnson, D. R. H., & Soderblom, D. R. 1987, AJ, 93, 864
Jönsson, H., Allende Prieto, C., Holtzman, J. A., et al. 2018, AJ, 156, 126
Jönsson, H., Holtzman, J. A., Prieto, C. A., et al. 2020, AJ, 160, 120
Kirby, E. N., Cohen, J. G., Smith, G. H., et al. 2011a, ApJ, 727, 79
Kirby, E. N., Guhathakurta, P., Bolte, M., Sneden, C., & Geha, M. C. 2009, ApJ, 705, 328
Kirby, E. N., Guhathakurta, P., Simon, J. D., et al. 2010, ApJS, 191, 352
Kirby, E. N., Lanfranchi, G. A., Simon, J. D., Cohen, J. G., & Guhathakurta, P. 2011b, ApJ, 727, 78
Kirby, E. N., Xie, J. L., Guo, R., et al. 2019, ApJ, 881, 45
Kleyna, J. T., Wilkinson, M. I., Evans, N. W., & Gilmore, G. 2004, MNRAS, 354, L66
Koch, A., Grebel, E. K., Gilmore, G. F., et al. 2008, AJ, 135, 1580
Koposov, S. E., Gilmore, G., Walker, M. G., et al. 2011, ApJ, 736, 146
Korotin, S. A., Andrievsky, S. M., Caffau, E., Bonifacio, P., & Oliva, E. 2020, MNRAS, 496, 2462
Lee, M. G., Yuk, I.-S., Park, H. S., Harris, J., & Zaritsky, D. 2009, ApJ, 703, 692
Lemasle, B., Hill, V., Tolstoy, E., et al. 2012, A&A, 538, A100
Lemasle, B., de Boer, T. J. L., Hill, V., et al. 2014, A&A, 572, A88
Letarte, B., Hill, V., Tolstoy, E., et al. 2010, A&A, 523, A17
Lucchesi, R., Lardo, C., Primas, F., et al. 2020, A&A, 644, A75
Majewski, S. R., Ostheimer, J. C., Kunkel, W. E., & Patterson, R. J. 2000a, AJ, 120, 2550
Majewski, S. R., Ostheimer, J. C., Patterson, R. J., et al. 2000b, AJ, 119, 760
Majewski, S. R., Schiavon, R. P., Frinchaboy, P. M., et al. 2017, AJ, 154, 94
Martin, N. F., de Jong, J. T. A., & Rix, H.-W. 2008, ApJ, 684, 1075
Mateo, M., Olszewski, E., Welch, D. L., Fischer, P., & Kunkel, W. 1991, AJ, 102, 914
McConnachie, A. W. 2012, AJ, 144, 4
Muñoz, R. R., Côté, P., Santana, F. A., et al. 2018, ApJ, 860, 66
Muñoz, R. R., Frinchaboy, P. M., Majewski, S. R., et al. 2005, ApJL, 631, L137
Nidever, D. 2021, dnidever/doppler: Cannon and Payne models, v1.1.0, Zenodo, doi:10.5281/zenodo.4906681
Nidever, D. L., Holtzman, J. A., Allende Prieto, C., et al. 2015, AJ, 150, 173
Nidever, D. L., Hasselquist, S., Hayes, C. R., et al. 2020, ApJ, 895, 88
Norris, J. E., Wyse, R. F. G., Gilmore, G., et al. 2010a, ApJ, 723, 1632
Norris, J. E., Yong, D., Gilmore, G., & Wyse, R. F. G. 2010b, ApJ, 711, 350
Norris, J. E., Yong, D., Venn, K. A., et al. 2017, ApJS, 230, 28
Ochsenbein, F., Bauer, P., & Marcout, J. 2000, A&AS, 143, 23
Okamoto, S., Arimoto, N., Tolstoy, E., et al. 2017, MNRAS, 467, 208
Osorio, Y., Allende Prieto, C., Hubeny, I., Mészáros, S., & Shetrone, M. 2020, A&A, 637, A80
Pace, A. B., Erkal, D., & Li, T. S. 2022, ApJ, 940, 136
Pace, A. B., Kaplinghat, M., Kirby, E., et al. 2020, MNRAS, 495, 3022
Palma, C., Majewski, S. R., Siegel, M. H., et al. 2003, AJ, 125, 1352
Pietrzyński, G., Górski, M., Gieren, W., et al. 2009, AJ, 138, 459
Pietrzyński, G., Gieren, W., Szewczyk, O., et al. 2008, AJ, 135, 1993
Plez, B., 2012 Turbospectrum: Code for Spectral Synthesis, Astrophysics Source Code Library, ascl:1205.004
Pont, F., Zinn, R., Gallart, C., Hardy, E., & Winnick, R. 2004, AJ, 127, 840
Queiroz, A. B. A., Anders, F., Chiappini, C., et al. 2020, A&A, 638, A76
Queiroz, A. B. A., Anders, F., Santiago, B. X., et al. 2018, MNRAS, 476, 2556
Ruiz-Lara, Tomás, Gallart, Carme, Bernard, Edouard J., & Cassisi, Santi 2020, NatAs, 4, 965
Santana, F. A., Beaton, R. L., Covey, K. R., et al. 2021, AJ, 162, 303
Santiago, B. X., Brauer, D. E., Anders, F., et al. 2016, A&A, 585, A42
Schlegel, D. J., Finkbeiner, D. P., & Davis, M. 1998, ApJ, 500, 525
Schönrich, R. 2012, MNRAS, 427, 274
Schönrich, R., Binney, J., & Dehnen, W. 2010, MNRAS, 403, 1829
Shetrone, M., Venn, K. A., Tolstoy, E., et al. 2003, AJ, 125, 684
Shetrone, M. D., Côté, P., & Sargent, W. L. W. 2001, ApJ, 548, 592
Simon, J. D., Jacobson, H. R., Frebel, A., et al. 2015, ApJ, 802, 93
Skúladóttir, Á., Andrievsky, S. M., Tolstoy, E., et al. 2015, A&A, 580, A129
Skúladóttir, Á., Tolstoy, E., Salvadori, S., Hill, V., & Pettini, M. 2017, A&A, 606, A71
Skúladóttir, Á., Salvadori, S., Amarsi, A. M., et al. 2021, ApJL, 915, L30
Smith, V. V., Bizyaev, D., Cunha, K., et al. 2021, AJ, 161, 254
Starkenburg, E., Hill, V., Tolstoy, E., et al. 2013, A&A, 549, A88
Suda, T., Yamada, S., Katsuta, Y., et al. 2011, MNRAS, 412, 843
Suda, T., Hidaka, J., Aoki, W., et al. 2017, PASJ, 69, 76
Suda, T., Katsuta, Y., Yamada, S., et al. 2008, PASJ, 60, 1159
Tafelmeyer, M., Jablonka, P., Hill, V., et al. 2010, A&A, 524, A58
Taylor, M. B. 2005, ASPC, 347, 29
Theler, R., Jablonka, P., Lucchesi, R., et al. 2020, A&A, 642, A176
Ural, U., Cescutti, G., Koch, A., et al. 2015, MNRAS, 449, 761
van der Walt, S., Colbert, S. C., & Varoquaux, G. 2011, CSE, 13, 22
Venn, K. A., Shetrone, M. D., Irwin, M. J., et al. 2012, ApJ, 751, 102
Vitali, S., Rojas-Arriagada, A., Jofré, P., et al. 2025, A&A, 699, A163
Walker, M. G., Mateo, M., & Olszewski, E. W. 2008, ApJL, 688, L75
Walker, M. G., Mateo, M., & Olszewski, E. W. 2009, AJ, 137, 3100
Walker, M. G., Olszewski, E. W., & Mateo, M. 2015, MNRAS, 448, 2717
Wang, S., & Chen, X. 2019, ApJ, 877, 116
Weisz, D. R., Dolphin, A. E., Skillman, E. D., et al. 2014a, ApJ, 789, 148
Weisz, D. R., Dolphin, A. E., Skillman, E. D., et al. 2014b, ApJ, 789, 147
Weisz, D. R., Dolphin, A. E., Skillman, E. D., et al. 2015, ApJ, 804, 136
Wenger, M., Ochsenbein, F., Egret, D., et al. 2000, A&AS, 143, 9
Westfall, K. B., Majewski, S. R., Ostheimer, J. C., et al. 2006, AJ, 131, 375
Wilkinson, M. I., Kleyna, J. T., Evans, N. W., et al. 2004, ApJL, 611, L21
Wilson, J. C., Hearty, F. R., Skrutskie, M. F., et al. 2019, PASP, 131, 055001
Wright, E. L., Eisenhardt, P. R. M., Mainzer, A. K., et al. 2010, AJ, 140, 1868
Yamada, S., Suda, T., Komiya, Y., Aoki, W., & Fujimoto, M. Y. 2013, MNRAS, 436, 1362
Yang, Y., Caffau, E., Bonifacio, P., et al. 2024, A&A, 691, A363
Zasowski, G., Cohen, R. E., Chojnowski, S. D., et al. 2017, AJ, 154, 198
Zasowski, G., Johnson, J. A., Frinchaboy, P. M., et al. 2013, AJ, 146, 81